SPECIAL
RELAMPAGO-CACTI
COLLECTION

Comparison of Biases in Warm-Season WRF Forecasts in North and South America

JEREMIAH O. PIERSANTE,[a] RUSS. S. SCHUMACHER,[a] AND KRISTEN L. RASMUSSEN[a]

[a] *Department of Atmospheric Science, Colorado State University, Fort Collins, Colorado*

(Manuscript received 23 April 2020, in final form 26 February 2021)

ABSTRACT: Ensemble forecasts using the WRF Model at 20-km grid spacing with varying parameterizations are used to investigate and compare precipitation and atmospheric profile forecast biases in North and South America. By verifying a 19-member ensemble against NCEP Stage-IV precipitation analyses, it is shown that the cumulus parameterization (CP), in addition to precipitation amount and season, had the largest influence on precipitation forecast skill in North America during 2016–17. Verification of an ensemble subset against operational radiosondes in North and South America finds that forecasts in both continents feature a substantial midlevel dry bias, particularly at 700 hPa, during the warm season. Case-by-case analysis suggests that large midlevel error is associated with mesoscale convective systems (MCSs) east of the high terrain and westerly subsident flow from the Rocky and Andes Mountains in North and South America. However, error in South America is consistently greater than North America. This is likely attributed to the complex terrain and higher average altitude of the Andes relative to the Rockies, which allow for a deeper low-level jet and long-lasting MCSs, both of which 20-km simulations struggle to resolve. In the wake of data availability from the RELAMPAGO field campaign, the authors hope that this work motivates further comparison of large precipitating systems in North and South America, given their high impact in both continents.

KEYWORDS: Complex terrain; Precipitation; Thunderstorms; Forecast verification/skill; Numerical weather prediction/forecasting; Convective parameterization

1. Introduction

North and South America are home to two of the world's largest mountain ranges: the Rocky and Andes Mountains. The elevation of these barriers, north–south orientation, and their position on the western side of the continents substantially influence the weather downstream because they modify midlatitude westerly and other associated flows. Interestingly, the regions east of the mountainous terrain in both continents are global hot spots for deep and organized convection, owing to the frequent occurrence of mesoscale convective systems (MCSs; Velasco and Fritsch 1987; Laing and Fritsch 1997; Houze 2004; Zipser et al. 2006; Houze et al. 2015).

Generally, convection initiation for MCSs in both continents involves the same key ingredients: 1) a poleward flux of low-level moisture from the Gulf of Mexico or the Amazon via the low-level jet (LLJ), 2) a capping inversion that prolongs the release of instability via westerly mid- to upper-level dry air subsidence from the high terrain, and 3) a lifting mechanism (Carlson et al. 1983; Maddox 1983; Laing and Fritsch 1997; Rasmussen and Houze 2011, 2016). A combination of these key ingredients east of the high terrain of the Rockies and Andes results in environments favorable for deep and organized convection in both continents, although some evidence suggests that extreme storms in South America may be deeper and more frequent than in North America (Zipser et al. 2006; Houze et al. 2015). Elevated mixed layers (EMLs) are also associated with hazardous weather with southwesterly upper-level flow over the high terrain in North America and northwesterly flow in South America due to an anomalously strong upper-level trough over the mountains (Rasmussen and Houze 2016; Cordeira et al. 2017; Ribeiro and Bosart 2018). These large clusters of thunderstorms produce various forms of severe weather with substantial socioeconomic impacts such as extreme rainfall and flooding, hail, strong winds, and tornadoes in both regions (Maddox 1980; Schumacher and Johnson 2005, 2006; Romatschke and Houze 2010; Rasmussen and Houze 2011; Cecil and Blankenship 2012; Rasmussen et al. 2014). Several previous studies show that MCSs contribute 30%–70% of warm-season precipitation in the United States (Fritsch et al. 1986; Durkee et al. 2009; Haberlie and Ashley 2019) and up to ~95% of summertime precipitation in subtropical South America. (Nesbitt et al. 2006; Romatschke and Houze 2010; Rasmussen et al. 2016).

However, despite the similarities in environmental conditions and storm impacts in both regions, there are several important differences among South American mesoscale features

Piersante's current affiliation: Department of Atmospheric and Environmental Sciences, University at Albany, State University of New York, Albany, New York.

Corresponding author: Jeremiah O. Piersante, jpiersante@albany.edu

DOI: 10.1175/WAF-D-20-0062.1

TABLE 1. BWW ensemble member setup employed for this study. All members were used for precipitation forecast evaluation; only CSU01 and CSU02 (italics) were used for atmospheric evaluation.

Member	LC/IBC	Cumulus	PBL	Microphysics
CSU01	GFS 0.5°	Kain–Fritsch	MYJ	Thompson
CSU02	GFS 0.5°	Grell–Freitas	MYJ	Thompson
ALB01	GFS 0.5°	Kain–Fritsch	MYJ	Thompson
ALB02	GEFSP01	Kain–Fritsch	MYJ	Thompson
ALB03	GFS 0.5°	Kain–Fritsch	YSU (top-down)	Thompson
ALB04	GFS 0.5°	Kain–Fritsch	ACM2	Thompson
ALB05	GFS 0.5°	New Tiedtke	MYJ	Thompson
ALB06	GFS 0.5°	Kain–Fritsch	YSU (top-down)	Thompson
ALB07	GFS 0.5°	Kain–Fritsch	GBM	Thompson
ALB08	GFS 0.5°	New Tiedtke	MYJ	Thompson
TTU01	GFS 0.5°	Tiedtke	YSU	Morrison
TTU02	GFS 0.5°	Tiedtke	MYNN	Morrison
TTU03	GFS 0.5°	Tiedtke	YSU	Thompson
TTU04	GFS 0.5°	Tiedtke	MYNN	Thompson
TTU05	GFS 0.5°	Tiedtke	YSU	WSM6
TTU06	GFS 0.5°	Tiedtke	MYNN	WSM6
PSU08	GFS 0.5°	Kain–Fritsch	YSU	Milbrandt–Yan
UND01	GFS 0.5°	Kain–Fritsch	MYJ	WSM6
UND02	GFS 0.5°	Grell–Freitas	YSU	Morrison

that suggest the convection of the region may be deeper and more frequent. For example, vertical heights of 40-dBZ convective echoes can range from 10 to 17 km across the warm season in subtropical South America where greater heights maximize near the Andes foothills (Rasmussen and Houze 2011). Furthermore, MCSs and their precipitation areas in South America tend to be substantially larger and longer-lived (Velasco and Fritsch 1987; Durkee et al. 2009) and occur over a smaller and more focused region east of the Andes Mountains in northern Argentina: the greater La Plata basin (Zipser et al. 2006; Romatschke and Houze 2010; Rasmussen et al. 2016). It is also common for the main convective area of South American MCSs in this region to propagate upstream, opposing the low-level jet and moisture flux (Anabor et al. 2008). These systems resemble a more robust version of the ''southward burst'' observed in North America (Porter et al. 1955; Stensrud and Fritsch 1993) as they can support convection lasting anywhere from 19 to 69 h (Anabor et al. 2008). This contrast is largely due to the complex terrain and deep LLJ of South America [referred to as the South American low-level jet (SALLJ)]. Though narrower, the Andes are approximately double the average altitude of the Rocky Mountains and block low to midtropospheric westerly flow, allowing for a much stronger northerly moisture flux along the terrain and enhanced lee cyclogenesis (Insel et al. 2010; Rasmussen and Houze 2016). Air then converges near the Andes foothills and the Sierras de Córdoba (SDC), a secondary north–south-oriented mountain range in northern Argentina, which provides enhanced lift to trigger deep convective cores and keep their western edge tied to the terrain while they grow upscale toward the east (Rasmussen and Houze 2011, 2016; Rasmussen et al. 2014). This ''back-building'' phenomenon leads to persistent convection and is unique to subtropical South America (Rasmussen et al. 2014).

Previous studies describe the relative depth and role of the SALLJ in convective initiation and contribution to regional rainfall (Marengo et al. 2002, 2004; Salio et al. 2002, 2007; Nascimento et al. 2016), but use LLJ identification criteria originally designed for North America (Bonner 1968) that neglects SALLJs in the La Plata basin that are elevated and/or feature a strong zonal component. Oliveira et al. (2018) created new criteria to address this shortcoming and found SALLJs often reach 700 hPa in and near the La Plata basin, making them much deeper than their North American counterpart, which tends to be maximized in the lowest 1 km above ground level (Smith et al. 2019; Hodges and Pu 2019). These findings are similar to those observed in Bolivia and western Paraguay during the South American Low-Level Jet Experiment (SALLJEX; Vera et al. 2006).

Given these impacts and complex initiation modes of MCSs, there is a serious demand for numerical weather prediction (NWP) to accurately represent and forecast such events. Unsurprisingly, convection-permitting models yield the most accurate forecasts, particularly when it comes to warm-season precipitation at long and short forecast lead times, such as the National Center for Atmospheric Research (NCAR) convection-allowing ensemble and the Storm Scale Ensemble Forecast system (Clark et al. 2009, 2012; Schwartz et al. 2015; Iyer et al. 2016). However, these simulations at 1–4-km horizontal resolution, or those truly resolving convection at ~100 m, can be computationally expensive (Weisman et al. 1997; Bryan et al. 2003; Petch 2006). As a result, convective parameterizations (CPs) are widely used with coarser resolutions for practical reasons, but carry inherent biases in precipitation forecasts (Davis et al. 2003; Jankov et al. 2005; Liu et al. 2006; Clark et al. 2007; Jeworrek et al. 2019).

Sensitivity of U.S. MCSs to CP choice within regional climate models has been noted in previous work, such as

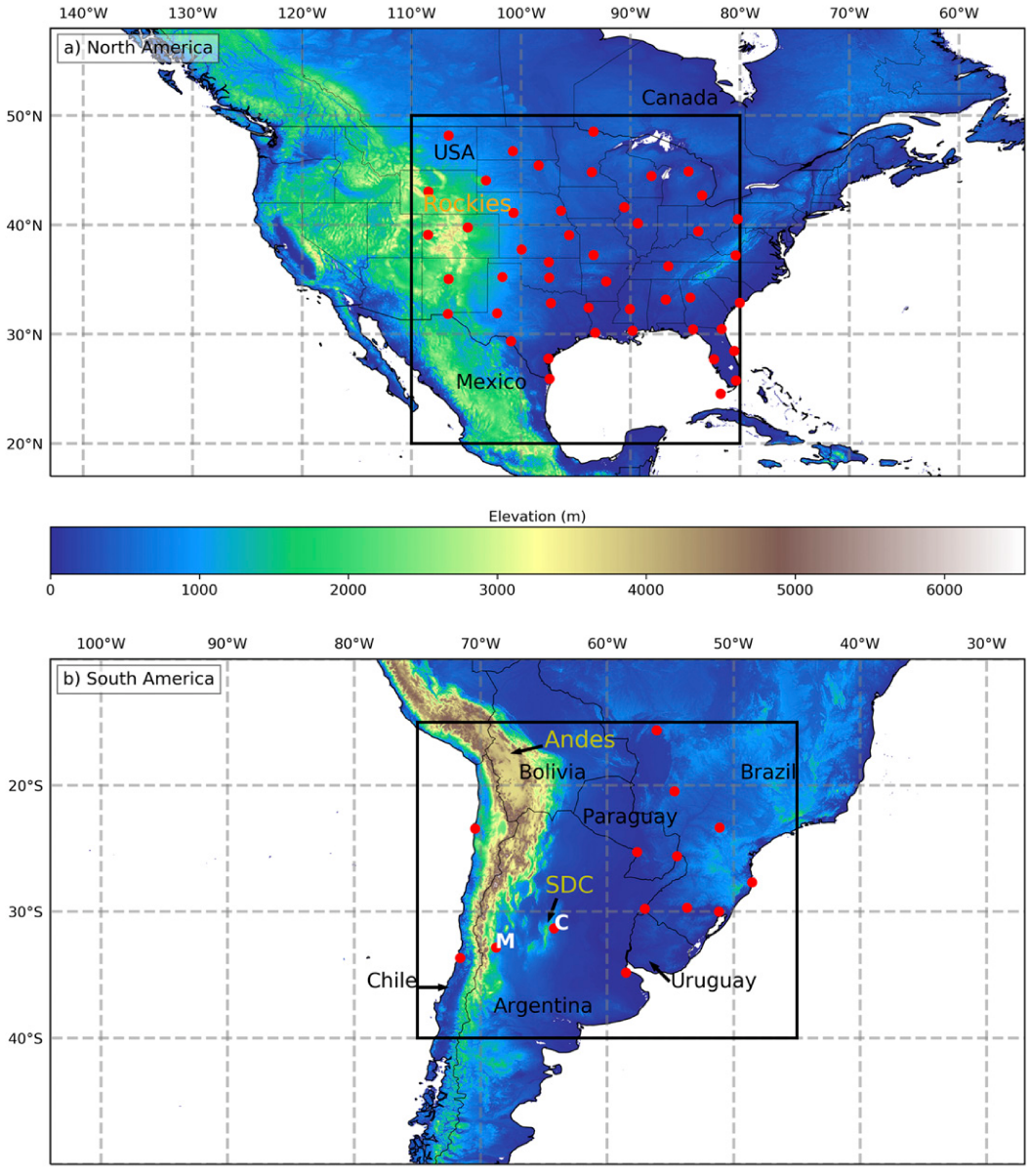

FIG. 1. (a) North and (b) South America model domains (entire panel), study domains for this work (black boxes), and radiosonde observation locations (red dots) used for this study. Topographic contours highlight the Rocky Mountains in (a) and the Andes Mountains and the Sierras de Córdoba (SDC) in (b). The letters M and C in (b) represent Mendoza and Córdoba cities.

Liang et al. (2012) with regard to the 1993 flooding event in the Mississippi River basin. Few studies, however, have investigated model performance and parameterization dependence in environments conducive to large precipitating MCSs in South America. Blázquez and Nuñez (2009) reaffirm that CPs have a large influence on accumulated warm-season precipitation, but they verify against reanalysis as opposed to in situ measurements and neglect to explore the accuracy of thermodynamic environment forecasts. Ruiz et al. (2010) show the tendency for models to underestimate SALLJ strength in addition to the influence of CPs and other parameterizations on precipitation and surface variables; however, this study lacks a direct comparison between CPs and surface variable biases. Müller et al. (2016) analyze precipitation and surface temperature forecasts over various forecast lead times, but use the same model configuration throughout.

Clearly, there has yet to be a robust model verification analysis of atmospheric conditions favorable for MCSs and extreme rainfall, such as temperature, relative humidity, and wind in South America. While surface observations are widespread and available for ensemble-based forecast verification

TABLE 2. Number of 24-h RH forecast observation/verification pairings at 0000 UTC per station in South America (all stations) and North America (most frequent 14 stations) during 4 Oct 2018–23 Feb 2019 and 1 May–30 Sep 2016, respectively.

South America			No. of monthly observations				
Lat (°)	Lon (°)	City	Oct	Nov	Dec	Jan	Feb
−29.70	−53.68	Santa Maria (SBSM)	22	30	31	29	21
−27.67	−48.55	Florianópolis (SBFL)	22	30	21	30	19
−20.47	−54.67	Campo Grande (SBCG)	22	30	31	29	20
−25.60	−54.48	Foz de Iguacu (SBFI)	22	29	31	30	21
−29.78	−57.03	Uruguaiana (SBUG)	21	25	28	28	21
−25.52	−49.17	Curitiba (SBCT)	21	27	30	29	20
−30.00	−51.18	Porto Alegre (SBPA)	18	30	31	29	21
−15.65	−56.10	Várzea Grande (SBCY)	17	20	25	19	17
−19.00	−57.67	Corumbá (SBCO)	10	0	0	0	0
−33.65	−71.62	Santo Domingo (SCSN)	5	28	26	28	21
−34.82	−58.53	Buenos Aires (SAEZ)	1	0	1	0	0
−32.83	−68.78	Mendoza (SAME)	0	29	14	0	0
−31.31	−64.21	Córdoba (SACO)	0	29	16	6	0
−27.45	−59.05	Resistencia (SARE)	0	2	0	0	0
		Total	181	309	285	257	181
North America			No. of monthly observations				
Lat (°)	Lon (°)	City	May	Jun	Jul	Aug	Sep
33.36	−84.57	Atlanta (KATL)	28	29	29	27	5
37.21	−80.41	Blacksburg (KBCB)	28	29	29	27	5
48.21	−106.63	Glasgow (KGGW)	28	29	29	27	5
39.77	−104.87	Denver (KDNR)	28	29	29	27	5
29.37	−100.92	Del Rio (KDRT)	28	29	29	27	5
30.45	−84.30	Tallahassee (TAE)	28	29	29	27	5
44.91	−84.72	Gaylord (APX)	28	29	29	27	5
39.42	−83.82	Wilmington (ILN)	28	29	29	27	5
42.70	−83.47	Detroit/Pontiac (DTX)	28	29	29	27	5
36.25	−86.56	Nashville (OHX)	28	29	29	27	5
32.84	−97.30	Fort Worth Meacham (KFTW)	28	29	29	27	5
31.94	−102.19	Midland (KMAF)	28	29	29	27	5
37.24	−93.40	Springfield–Branson (KSGF)	28	29	29	27	5
44.50	−88.11	Green Bay NWS (KGRB)	28	29	29	27	5
		Total	392	406	406	378	70

of extreme rainfall and the associated environmental characteristics in North America (Schumacher and Davis 2010; Schumacher and Clark 2014), there is a significant lack of consistent and available observation data in South America, creating challenges in verifying operational model data in this region and also assimilating observations into models to improve their performance. Fortunately, field campaigns such as SALLJEX (Vera et al. 2006) and RELAMPAGO (Nesbitt et al. 2021) in north-central Argentina provide useful observational data. The latter ensured that most surface stations in Argentina were functioning throughout the campaign, which took place November–December 2018.

The primary goal of this study is to evaluate and compare model forecasts of atmospheric conditions during boreal and austral warm seasons of North and South America, respectively, considering the potential impacts of subsident flow and the LLJ on convective, heavily precipitating systems set forth by previous work. First, we examine the effects of CP on precipitation forecasts in North America, using a multisensor gridded precipitation analysis. Second, we use multiple CPs to assess atmospheric profile forecast error and address the spread between them. We end with investigating interesting cases in each continent to test our hypotheses and exemplify our results.

2. Methodology

This study consists of three parts: 1) precipitation forecast evaluation in North America, 2) atmospheric profile forecast evaluation in both North and South America, and 3) analysis of North and South American cases based on results in 2).

a. Precipitation forecast evaluation

Model statistics on precipitation forecast accuracy are calculated over a domain covering the contiguous United States (CONUS). The Big Weather web (BWW; Maltzahn et al. 2016) ensemble, which was a distributed ensemble run at seven U.S. universities, included 47 members with perturbations to the initial conditions and physical parameterizations. The ensemble was not optimized for probabilistic forecasting, but instead to allow for evaluations of the effects of various

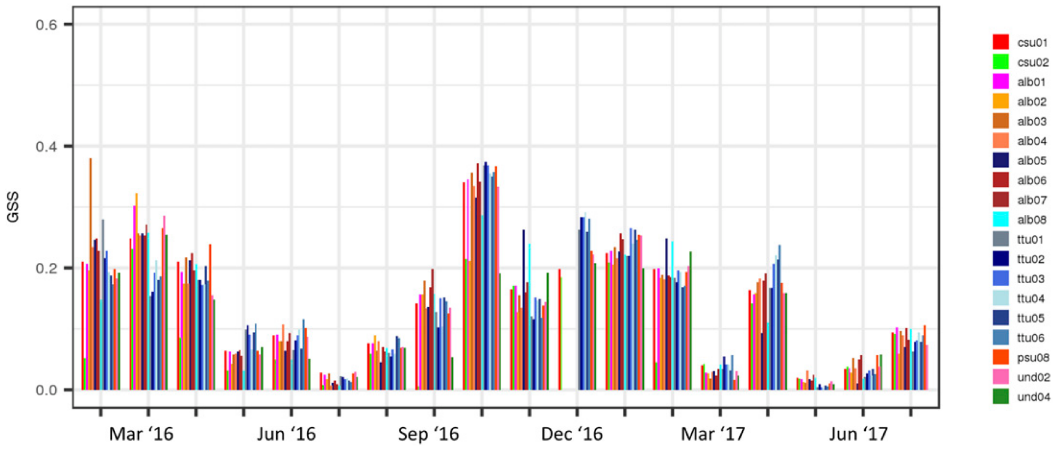

FIG. 2. Gilbert skill score (GSS) for 36–60-h QPF 50.8-mm threshold over CONUS for the members shown in Table 1 during February 2016–July 2017. Color distinguishes CP: warm colors indicate KF, green indicates GF, and blue indicates Tiedtke. Several BWW members were unable to be run for December 2016.

perturbations over many members and a consistent period of study. In other words, the emphasis of the BWW ensemble is to determine the impact of physical parameterizations on forecast skill as opposed to probabilistic forecast uncertainty and reliability. Other multiphysics ensembles, such as the Community Leveraged Unified Ensemble (Clark et al. 2018), have also been employed to optimize convection-allowing model configurations rather than focusing on probabilistic forecasting.

In this study, we use a subset of the BWW ensemble to compare forecasts with respect to varying parameterizations (e.g., CP, microphysics, PBL) rather than uncertainty from initial condition or stochastic perturbations. In particular, the ensemble subset used here consists of 19 members with 20-km grid spacing initialized daily at 0000 UTC from February 2016 to July 2017. Though the focus of this work is to identify warm season error, cool season months were included to highlight how precipitation forecast skill is lowest during the warm season; the change in error with season is discussed throughout the paper. All members were run via the Advanced Research version of the Weather and Forecasting (WRF) Model (Skamarock et al. 2008) version 3.7.1 with RRTMG radiation (Iacono et al. 2008), Noah land surface (Tewari et al. 2004), 43 vertical levels, a 90-s time step, and GFS initial/lateral boundary conditions (except for one that uses GEFS), but each member uses a different combination of physical parameterizations (cumulus, PBL, microphysics). Cumulus schemes include Kain (2004) and Grell and Freitas (2014), New Tiedtke (Zhang and Wang 2017), and Tiedtke (Zhang et al. 2011). Microphysics schemes include Thompson et al. (2008) and Morrison et al. (2009), and WRF single-moment 6-class microphysics scheme (WSM6; Hong and Lim 2006); Milbrandt and Yau (2005). Planetary boundary layer (PBL) schemes include Yonsei University scheme (YSU; Hong et al. 2006), Mellor–Yamada–Janjić scheme (MYJ; Janjić 1994), asymmetric convection model 2 scheme (ACM2; Pleim 2007), Grenier–Bretherton–McCaa scheme (GBM; Grenier and Bretherton 2001), and Mellor–Yamada–Nakanishi–Niino level 2.5 scheme (MYNN; Nakanishi and Niino 2009). The ensemble setup is summarized in Table 1; the first two members are also used in the atmospheric profile evaluation. CSU01 and ALB01 are each run despite having identical physical parameterizations because it has been found that using different computing systems alone can lead to discrepancies among simulations (Tao and Zhang 2015).

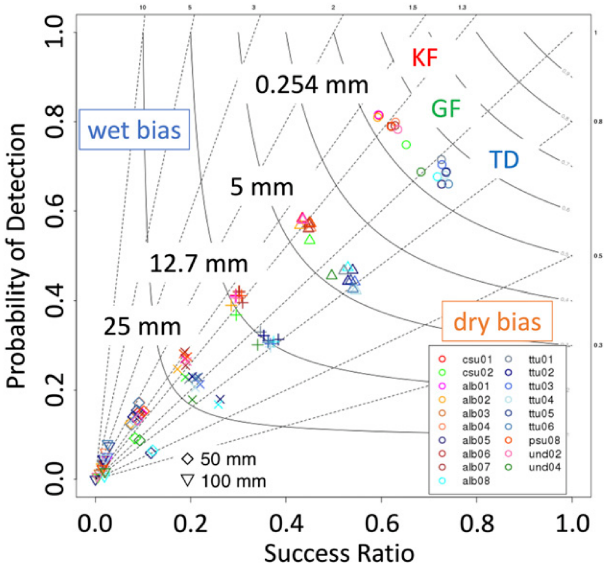

FIG. 3. Roebber performance diagrams of 36–60-h ensemble member forecasts at various precipitation amounts over CONUS during 2016 and 2017 warm season months (May–August). The shapes distinguish precipitation amount, and color indicates CP as in Fig. 2. Areas where the success ratio is greater than the probability of detection is labeled with "dry bias" in orange text. Oppositely, "wet bias" in blue text is labeled where the probability of detection is greater than the success ratio.

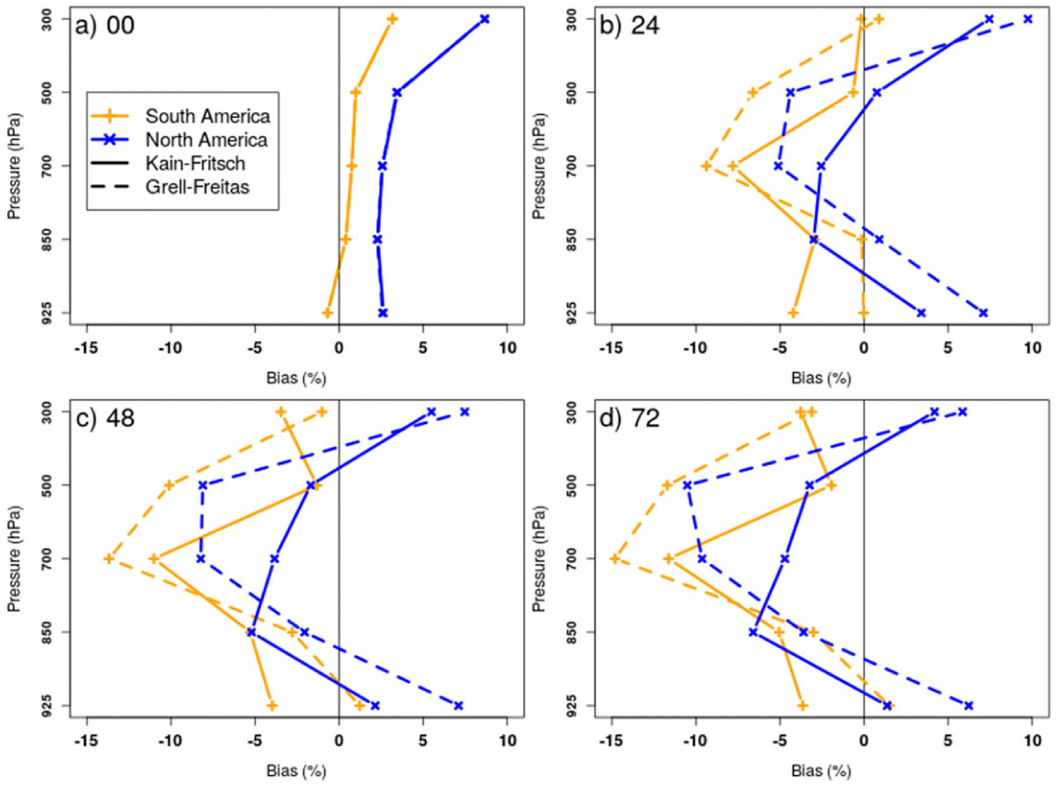

FIG. 4. Mean RH forecast bias at various pressure levels (vertical axes) at forecast lead times of (a) 0, (b) 24, (c) 48, and (d) 72 h. Yellow (blue) indicates South America (North America), and solid (dashed) lines indicate Kain–Fritsch (Grell–Freitas) cumulus parameterization. Biases were calculated by averaging all available stations in the respective domain and warm seasons (4 Oct 2018–23 Feb 2018 for South America; 1 Apr 2016–30 Sep 2016 for North America).

The authors used METv8.0 (Gotway et al. 2018) to verify precipitation forecasts against NCEP Stage-IV analyses (Lin and Mitchell 2005), regridded to the BWW forecast grid. Quantitative precipitation forecasts (QPFs) were evaluated on a grid-by-grid basis using the Gilbert skill score (GSS; see Gotway et al. 2018) and Roebber performance diagrams (Roebber 2009). GSS measures how well forecast "yes" precipitation events correspond to observed "yes" events, taking into account random chance:

$$\mathrm{GSS} = \mathrm{hits} - \frac{\mathrm{hits}_{\mathrm{random}}}{\mathrm{hits} + \mathrm{misses} + \mathrm{false\ alarms} - \mathrm{hits}_{\mathrm{random}}}, \quad (1)$$

where

$$\mathrm{hits}_{\mathrm{random}} = \frac{\mathrm{hits} + \mathrm{false\ alarms}}{\mathrm{hits} + \mathrm{misses}}/\mathrm{total}, \quad (2)$$

and a hit is an accurate forecast "yes" on a grid, a miss is a forecast "no" on an observed "yes", and a false alarm is a forecast "yes" on an observed "no." GSS ranges from $-1/3$ to 1 with 0 indicating zero skill and 1 perfect skill. The Roebber performance diagram is used to simultaneously plot success ratio (SR; 1 − false alarm ratio) and probability of detection (POD), and also reveals the critical success index (CSI) and frequency bias. Here, greater skill is represented by an increase in these ratios at 45°. An instance in which POD > SR indicates a wet model bias, and the opposite for a dry bias.

An identical analysis is not possible in South America due to a lack of a suitable high-resolution multisensor precipitation analysis in the region. This is an interesting area for future work; however, the precipitation evaluation results in North America adequately motivate the atmospheric forecast evaluation (methodology outlined below).

b. *Atmospheric profile forecast evaluation*

Routine evaluation of daily BWW forecasts over CONUS indicated there were substantial differences in upper-level temperature and humidity between ensemble members with different CPs. Given this finding and the availability of members at Colorado State University, the authors selected CSU01 and CSU02 with Kain–Fritsch (KF) and Grell–Freitas (GF) CPs, respectively, for the atmospheric profile evaluation in North and South America (Table 1). CSU01 and CSU02 in North and South America are identical except for the domain, WRF version (3.8 in South America), and timeframe, as South America runs were initially used for forecasting during the

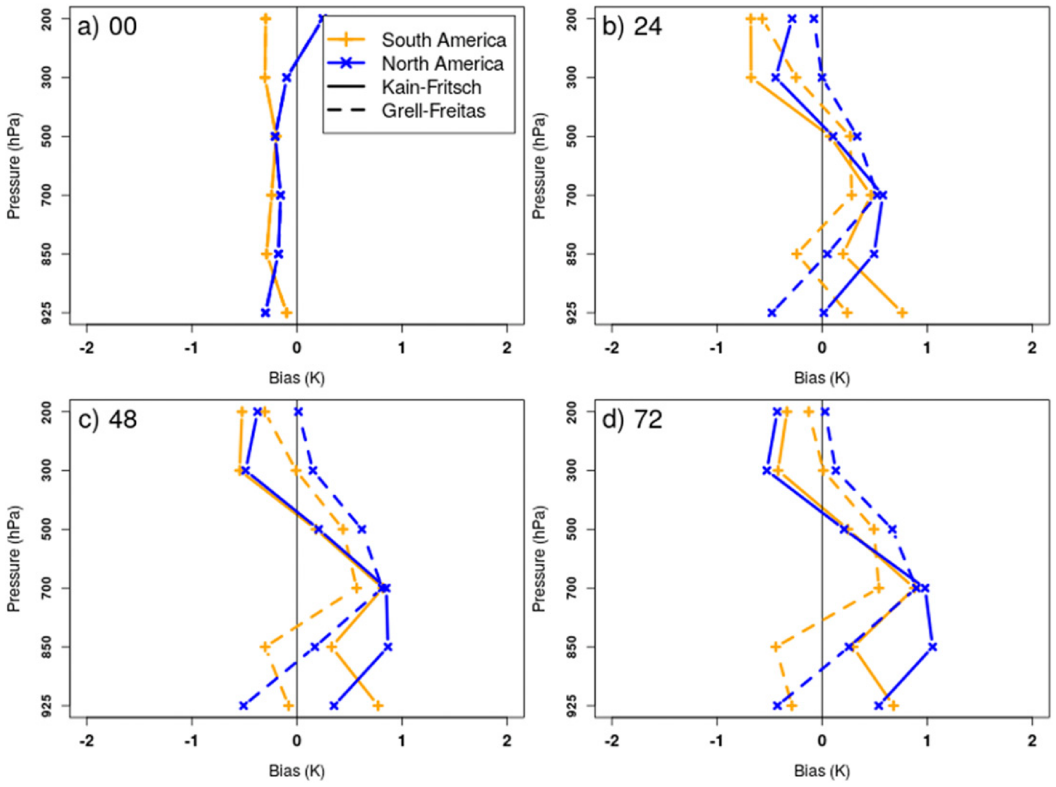

FIG. 5. As in Fig. 4, but for mean temperature bias. Note that 200 hPa was available for temperature but not RH.

RELAMPAGO field campaign from 4 October 2018 to 23 February 2019. The atmospheric profile forecast analysis in section 4 focuses on the comparison of this 2018/19 South America warm season to the 2016 North America warm season (initializations from 1 May to 30 September).

Forecasts were verified against operational radiosonde observations occurring daily at 0000 and 1200 UTC (Satellite Services Division/Office of Satellite Data Processing and Distribution/NESDIS/NOAA/U.S. Department of Commerce, and National Centers for Environmental Prediction/National Weather Service/NOAA/U.S. Department of Commerce 2004). These observation locations, topographic features, and other notable landmarks in each continent are presented in Fig. 1. Both study domains capture the Rocky and Andes Mountains in the west, the plains in the east, and the coastal regions of the Gulf of Mexico and the Atlantic. While the Rockies are wider, the Andes are approximately twice as tall. The SDC is highlighted east of the high terrain in addition to Mendoza and Córdoba cities, all of which were major focal points of RELAMPAGO (Fig. 1b). South America clearly has fewer observation stations than North America (Fig. 1a). Furthermore, most South America locations lacked consistent daily 0000 UTC observations (Table 2). This was particularly the case for locations in Argentina; Mendoza and Córdoba sites halted

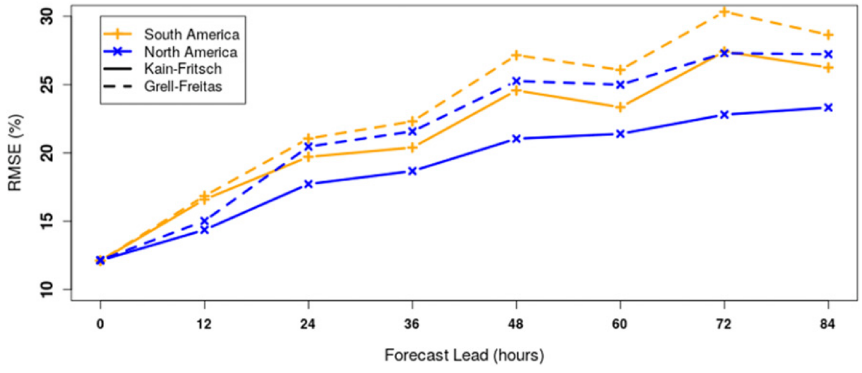

FIG. 6. Root-mean-square error (RMSE) for 700-hPa relative humidity at various forecast lead times, in hours. Colors and line styles match those described in Fig. 4.

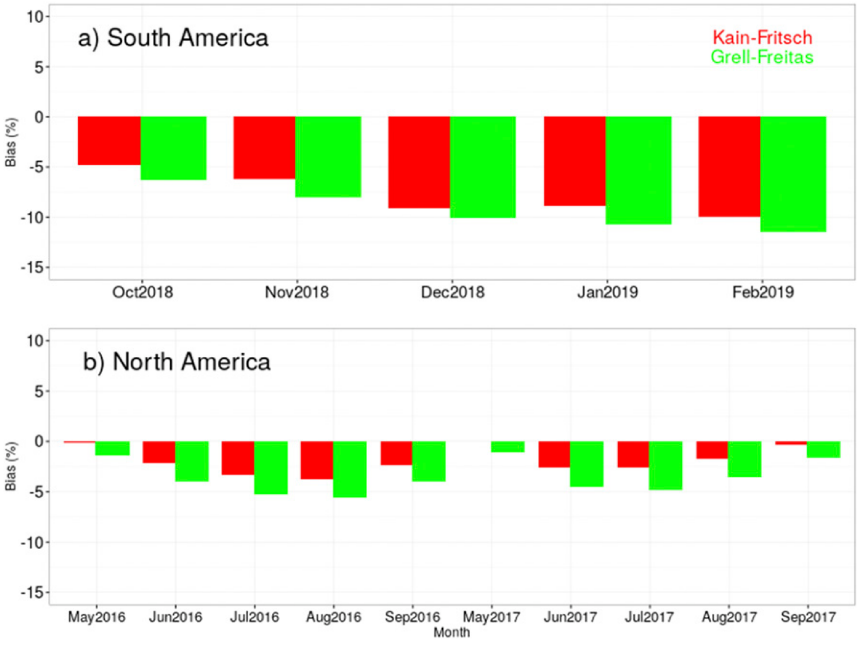

FIG. 7. Average monthly RH bias for 24-h 700-hPa forecasts using Kain–Fritsch (red; left bars) and Grell–Freitas (green; right bars) in (a) South America and (b) North America during warm-season months.

observations at the conclusion of RELAMPAGO's intensive observation period in mid-December. September 2016 in North America also had very few 0000 UTC observation/verification pairings a result of the failure to initialize the model throughout most of the month. There were additional instances in which other BWW simulations were not run in North America such as December 2016, which can be identified in the precipitation analysis (section 3). We focus on 0000 UTC verification times as this is when most stations tended to take observations, but a few, such as Buenos Aires, performed most at 1200 UTC.

We focus our analysis on relative humidity (RH) and temperature at various pressure levels throughout the atmosphere, enabling a model bias assessment of thermodynamic environments that could influence MCSs and large-scale precipitation events. While RH is not an absolute moisture variable as it depends on temperature, it best represents the impacts of clouds and convection, which is what the CP attempts to describe. We also assess meridional wind (v-component wind) to identify potential LLJ errors.

METv8.0 was also implemented to calculate point verification statistics, namely the bias and root-mean-square error (RMSE):

$$\text{bias} = \text{forecast} - \text{observation}, \tag{3}$$

$$\text{RMSE} = \sqrt{\frac{1}{n}\sum_{i}^{n}(\text{forecast} - \text{observation})^2}. \tag{4}$$

Following the North America precipitation forecast evaluation in section 3, we first compare RH and temperature profile biases between continents and CPs at various forecast lead times. We then assess the temporal evolution of RH error with respect to lead time and month, followed by the spatial distribution of the RH and meridional wind error among similar North and South America months.

c. *North and South American case analysis*

Last, we highlight particular events in each warm season with substantial errors (or lack thereof) and attempt to diagnose the probable causes of each. For South America, we choose an MCS case during RELAMPAGO given its complex structure, spatial and temporal extent, likelihood of inducing widespread forecast error, and data availability. It also featured elements of upstream propagation, a phenomenon described by Anabor et al. (2008). Helpful tools and resources used for this analysis include the NOAA Hybrid Single-Particle Lagrangian Integrated Trajectory model (HYSPLIT[1]; Stein et al. 2015) for determining parcel backward trajectories via GDAS 1° reanalysis in addition to *GOES-16* infrared (IR) temperature, Read/Interpolate/Plot V 4.7 (RIP; Stoelinga et al. 2018) for calculating and plotting backward trajectories of WRF output, and NEXRAD radar archive imagery (see the data availability statement) for storm identification in South and North America, respectively.

3. Precipitation forecast evaluation in North America

GSS of 36–60-h QPF, especially for 50.8 mm over CONUS, has a clear seasonal dependence (Fig. 2), maximizing in the

[1] https://www.ready.noaa.gov/HYSPLIT_traj.php.

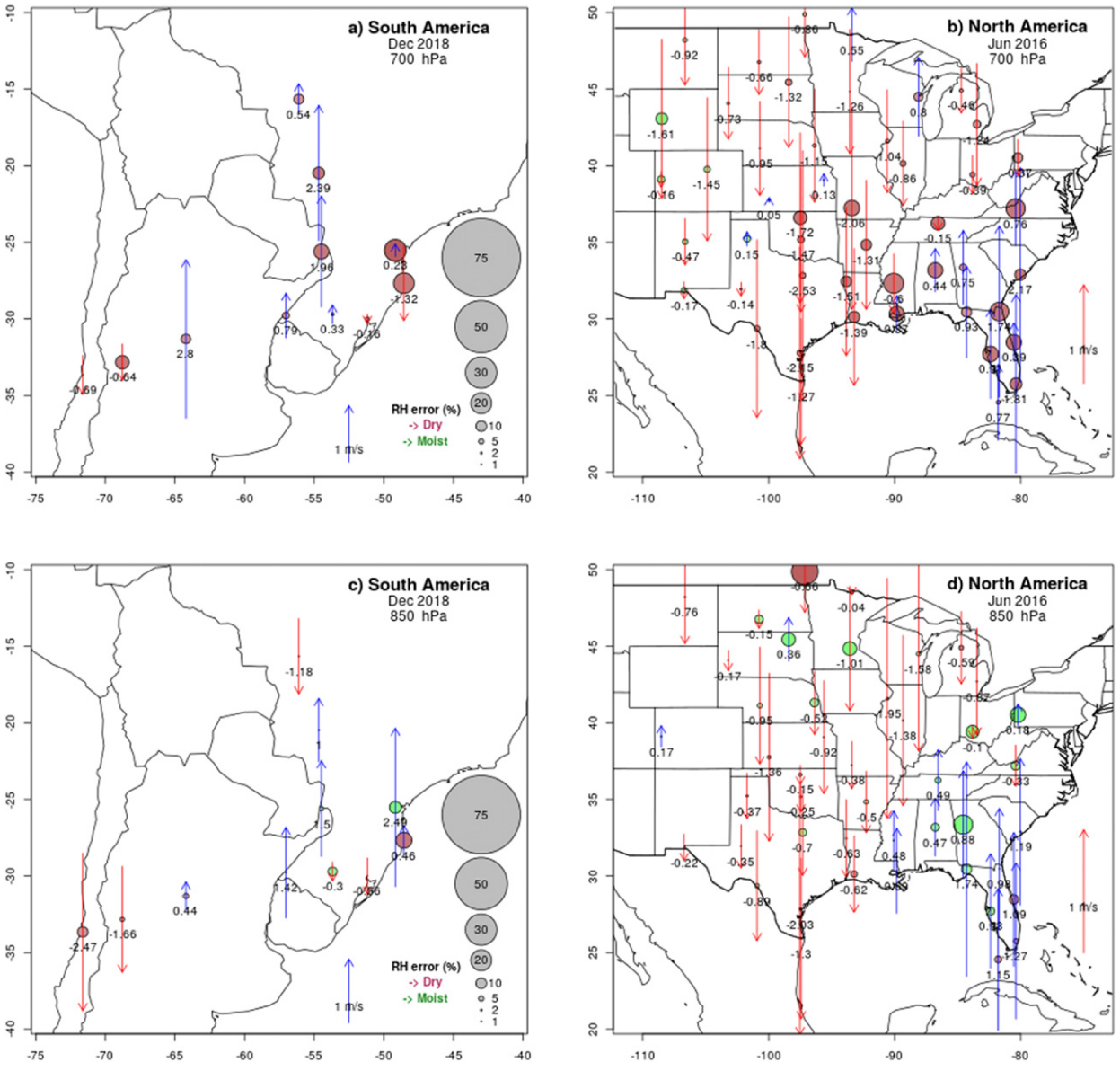

FIG. 8. Monthly average 24-h relative humidity and meridional wind forecast biases at (a),(b) 700 hPa and (c),(d) 850 hPa in (left) South America (December 2018) and (right) North America (June 2016) at available sounding locations using the Grell–Freitas cumulus parameterization. Red (green) indicates a dry (wet) RH model bias and size of the sounding location represents the magnitude. Arrow direction and length indicate the sign and magnitude of meridional wind error; the number at each station gives the actual meridional wind bias rounded to the nearest hundredth meter per second. Color further distinguishes meridional wind bias direction: blue (red) represents positive/northward (negative/southward) model bias. Only locations with multiple 0000 UTC verification times throughout the month are included.

cool months (e.g., October 2016) and minimizing in the warm months (e.g., July 2016 and May 2017). Most notably, the Tiedtke CP had greater skill in the 2016/17 cool months (Fig. 2). Members with the same CP also tended to cluster together. GSS values were higher for 12–24-h forecasts and lower for 60–72-h forecasts, but similar clustering behavior was evident at these forecast leads as well (not shown).

Focus is shifted to only the warm season (May–August) when forecast skill was clearly the lowest. Unsurprisingly, forecast skill was greatest at lower precipitation amounts (Fig. 3). Ensemble members of the same CP also cluster together because most warm-season precipitation is convective, and thus the CP scheme has a greater influence on precipitation forecasts than in the cool season. (Fig. 3). In contrast, there is much less evidence of clustering associated with other parameterizations. Among CP schemes, KF members featured a wet bias at all precipitation amounts. Tiedtke members on the other hand were less biased at lower amounts. New Tiedtke

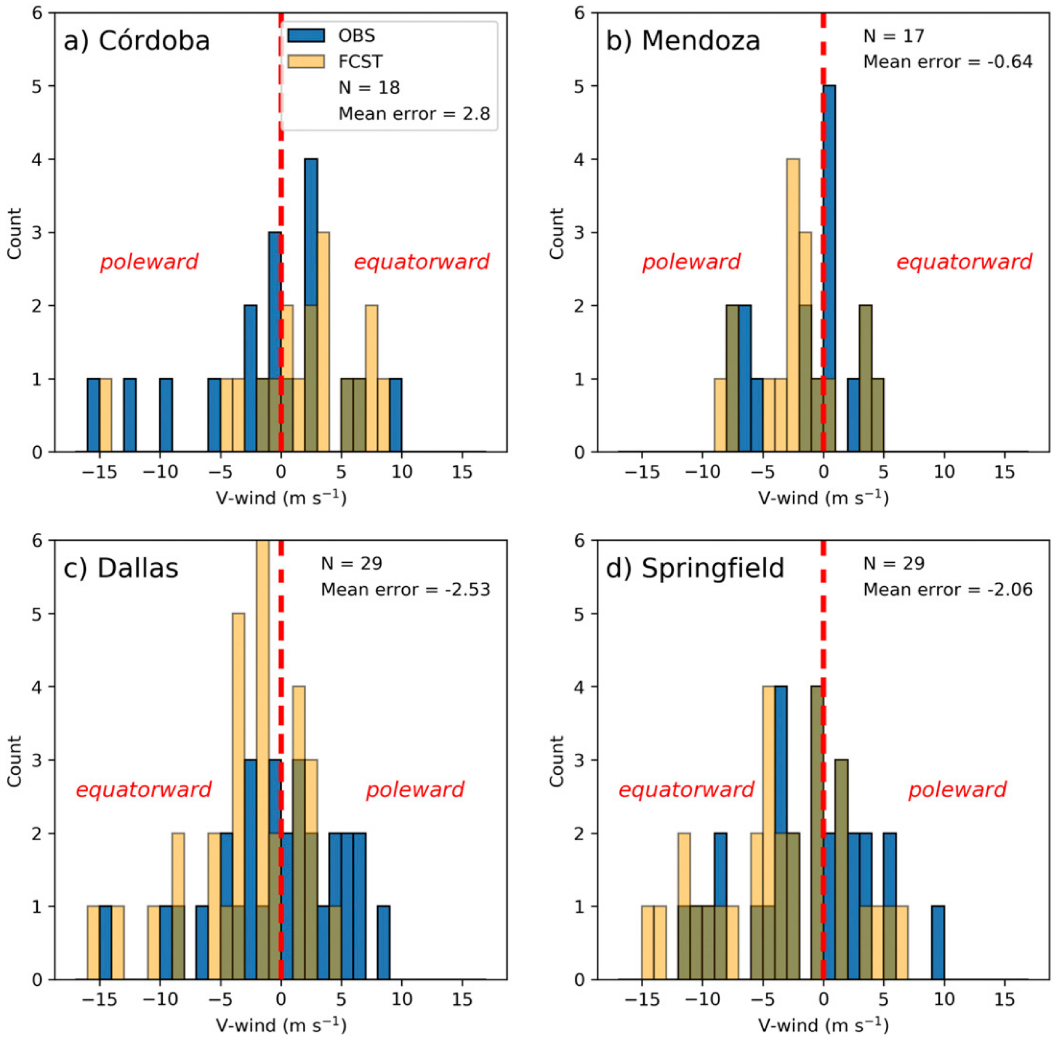

FIG. 9. Meridional wind observation (blue) and forecast (yellow) distribution for South American cities (a) Córdoba, Argentina, and (b) Mendoza, Argentina, and North American cities (c) Dallas, TX, and (d) Springfield, MO, during December 2018 and June 2016, respectively. The olive shading represents the overlap between the observation and forecast. Positive (negative) meridional wind is northward (southward), indicated by the red text and separated by a red-dashed line at 0 m s^{-1}. The number of observation/forecast pairings N in addition to the mean error (m s^{-1}) as shown in Fig. 8 is also given for each city.

members (ALB08 and ALB05) were fairly dry at higher amounts, however (Fig. 3). GF members fell between KF and New Tiedtke members at all amounts. These results are similar to those in Jeworrek et al. (2019) where choice of CP was found to have a key influence on precipitation patterns during convective events in the southern Great Plains of the United States.

CP has the most evident influence on precipitation forecasts compared to other parameterizations in Table 1, a conclusion also drawn in Jeworrek et al. (2019). Acknowledging these CP biases is crucial from a forecasting and regional climate analysis standpoint; depending on the application, it might be preferable to be unbiased at high amounts and accept the high bias at low amounts, or alternatively to be unbiased at low amounts that are more frequent.

Though we did not perform an identical analysis in South America, Blázquez and Nuñez (2009) have shown warm-season precipitation forecasts in South America are also substantially impacted by the choice of CP. In section 4, we begin the comparison of atmospheric profile forecast biases between North and South America using KF and GF CPs. This allows for identifying differences in bias characteristics associated with these CPs between the different regions.

4. Atmospheric profile evaluation in North and South America

a. *Profile biases*

RH forecast bias, averaged across the 2018/19 (South America) and 2016 (North America) warm seasons, is strongly

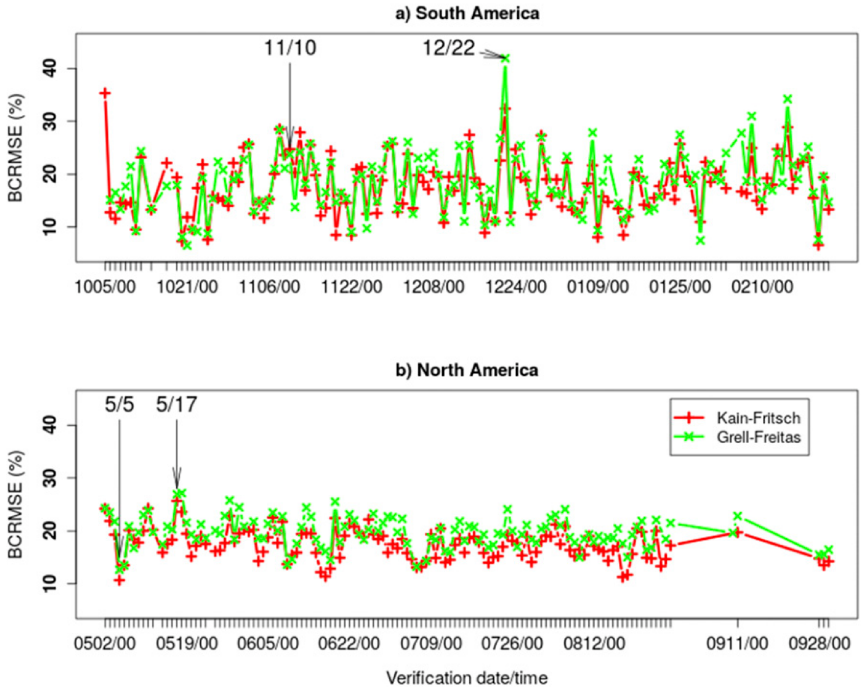

FIG. 10. Mean 700-hPa 24-h RH forecasts in (a) South America and (b) North America. Red (green) indicates Kain–Fritsch (Grell–Freitas).

influenced by continent, CP, and forecast lead time (Fig. 4). Upon model initialization, a slight wet bias already existed at all levels except for at 925 hPa in South America (Fig. 4a). CPs were equal at this time since there had been zero model spinup; errors are differences between the GFS initial conditions and the point observations.

With a 24-h forecast lead, the midlevels, namely 700 hPa, were too dry with the greatest overall bias in South America and with GF approaching −10% (Fig. 4b). One continental contrast is that North America featured a wet bias at 925 and 300 hPa for both CPs, where South America was slightly too dry at 925 hPa and nearly unbiased at 300 hPa (Fig. 4b). These trends became more robust with 48- and 72-h leads: South America GF was nearly −15% at 700 hPa with South America KF not far behind (Figs. 4c,d). In general, a midlevel dry bias grew with increased lead time and error maximized in South America and with GF.

There are also notable temperature biases within both continents (Fig. 5). Both continents featured a slight cool bias at most levels upon initialization, and like RH, bias was equal among CPs (Fig. 5a). At 24 h, all demonstrated a warm bias slightly less than 1 K at 700 hPa (Fig. 5b), becoming greater, particularly for North America runs, at longer forecast leads (Figs. 5c,d). There was less agreement aloft and near the surface, however. GF was nearly unbiased at 200 and 300 hPa where KF was slightly cool for both North and South America. North America KF was the warmest at 850 hPa, but there was no clear worst performer at 925 hPa (Figs. 5c,d). These results are quite different from those in Grell and Freitas (2014) who found a low-level cool and moist bias and an upper-level warm and dry bias for South America Forecasts also using 20-km GF schemes (their Fig. 14). Their verification, however, only focused on a 15-day period in January over the Amazon—the predominant moisture source of the subtropics. The domain in the current study on the other hand relies on the southward advection of moisture from the Amazon via the SALLJ, a process we hypothesize that 20-km models struggle representing and thus likely explaining the discrepancy in GF atmospheric profile verification.

This consistent midlevel warm bias partially explains the midlevel low RH bias in Fig. 4, given that increasing temperature with constant moisture decreases RH. Interestingly, however, North America KF had the warmest bias here (Fig. 5d) yet South America GF had the driest (Fig. 4d). Furthermore, a warm bias did not always coincide with a dry bias, as seen with South America runs at 300 hPa at 24-h (Figs. 4b and 5b). For the remainder of this study, we focus on this bias maximum at 700 hPa and attempt to explain its probable causes. This level is important for models to accurately represent because the SALLJ transports a nonnegligible amount of moisture toward the region of convective development even this high in the atmosphere.

b. Relative humidity temporal variation

As seen in Figs. 4 and 5, forecast lead time influences temperature and RH bias. The overall error (RMSE) for 700-hPa RH forecasts grows with increased lead time (Fig. 6). All runs on average begin with 12% RMSE upon initialization, and increase to anywhere from 21% to 30% as lead increases to

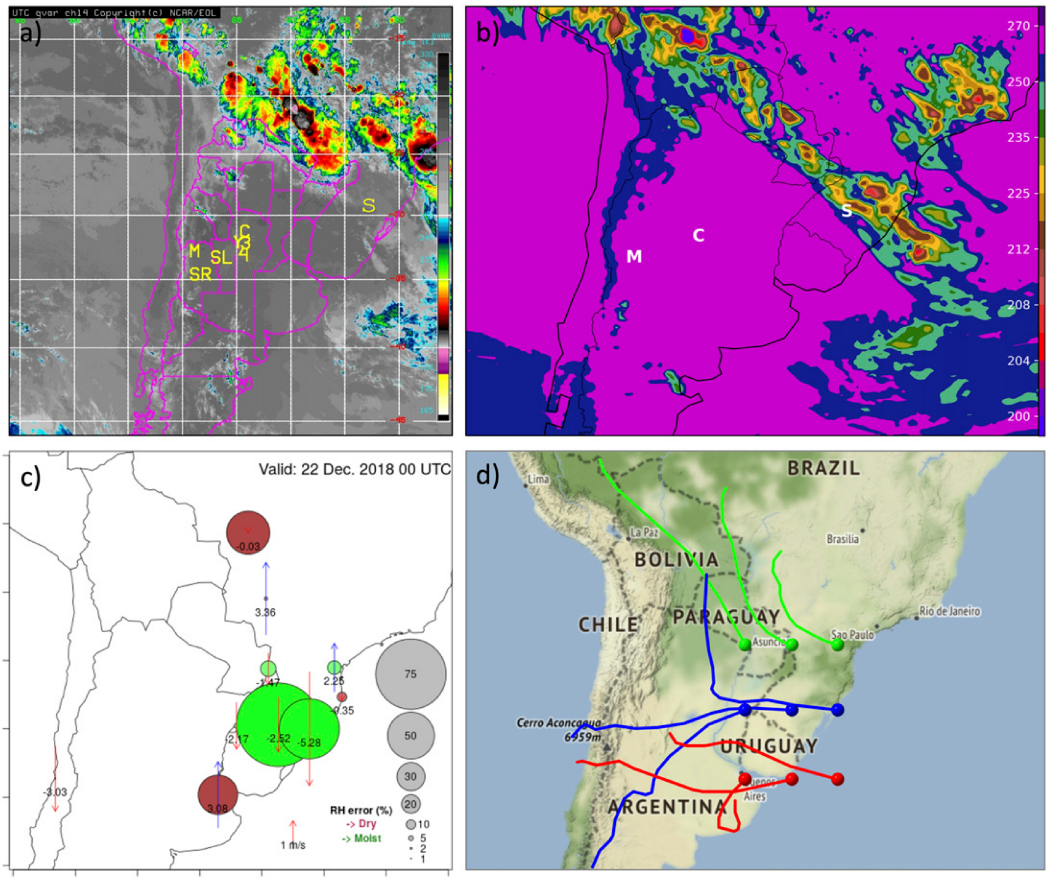

FIG. 11. The 0000 UTC 22 Dec 2018 case: observation vs forecast. (a) *GOES-16* IR temperature, (b) WRF simulated IR temperature using GF and 24-h forecast lead, (c) 700-hPa RH and meridional wind bias as in Fig. 8b but for the one verification time at 0000 UTC 22 Dec 2018, and (d) GDAS 1° reanalysis 48-h backward trajectories ending at 0000 UTC via NOAA HYSPLIT model. In the backward trajectories, colors differentiate parcels ending at the same latitude. M, C, and S in (a) and (b) indicate locations of Mendoza, Córdoba, and Santa Maria cities. More local landmarks are also marked in (a): SR, San Rafael; SL, San Luis; Y, Villa Yacanto; 3, Río Tercero; and 4, Río Cuarto.

84 h. Again, more error occurs in South America and with GF. The increase in RMSE is smaller from 0000 to 1200 UTC verification (e.g., 24–36 h), and even is a decrease with South America longer lead times. This is likely influenced by morning versus evening verification and fewer 1200 UTC observations available in South America.

Both warm season months in North and South America featured substantial 700-hPa dry biases, where GF was more biased than KF and South America was more biased than North (Fig. 7). This bias maximized at the end of the South American warm season (Fig. 7a) and the middle of North American warm seasons (Fig. 7b). The enhanced bias during South America's February was likely due to a lack of active sounding stations, and thus a smaller sample size, within the domain in the latter half of this warm season; the impacts of an inconsistent sample size are discussed further within the context of a particular case in section 5. To summarize, substantial midlevel dry bias was prominent in North and South American warm seasons, when deep convection is most frequent and the CP schemes are presumably most active. Interestingly, this error was greater in South America.

c. *Relative humidity and meridional wind spatial variation*

December 2018 and June 2016 for South and North America, respectively, exemplified the warm season bias mentioned above and consisted of enough observations to make direct comparisons between continents (Table 2). The following results were similar for KF and GF, but we present GF biases particularly at 24 h as they already exceeded 20% RMSE (Fig. 6) and were greater overall. On average, 24-h forecasts for 700-hPa RH using GF were too dry at almost every location in South America, many of which exceeded 20% (Fig. 8a). Most sites also featured an equatorward meridional wind bias, thus underrepresenting the SALLJ and the poleward moisture flux. Closer to the high terrain, Córdoba on average also featured a strong equatorward meridional wind bias ($2.8\,m\,s^{-1}$) in association with a ~10% dry bias. Mendoza on the other hand had a greater dry bias in tandem with a slight poleward

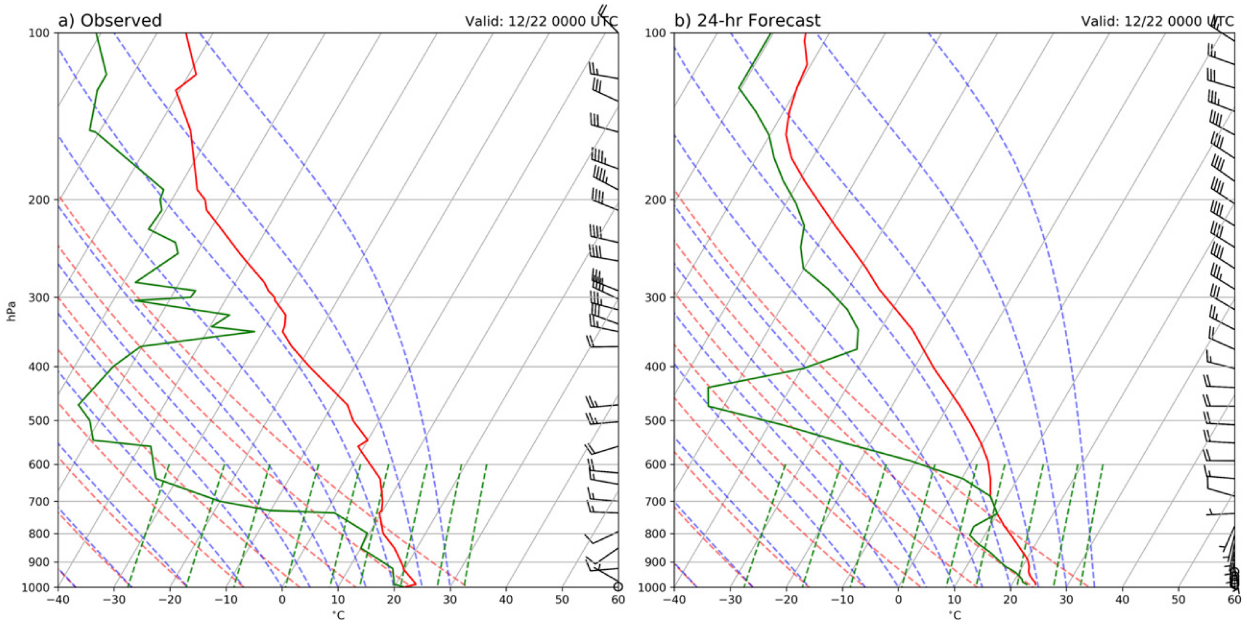

FIG. 12. Observed (a) and Grell–Freitas forecasted (b) Santa Maria soundings valid at 0000 UTC 22 Dec 2018. Pressure (hPa) and temperature (°C) serve as the vertical and horizontal coordinates, respectively. Wind barbs on the right of each skew T–log$p$ diagram indicate direction and speed, where a long tick represents 10 m s^{-1} and a short tick represents 5 m s^{-1}. Temperature (dewpoint temperature) is plotted in red (green). Moist adiabats, dry adiabats, and mixing lines are represented by dashed lines of blue, red, and green, respectively.

meridional wind bias (Fig. 8a). Its proximity to the Andes Mountains is likely a key influence on this difference as the topography, and thus the wind, is smoothed in the model simulation.

June 2016 in North America was very similar: all locations featured a dry bias east of the elevated terrain (~100°W), and with the exception of the Southeast United States, there was a widespread equatorward meridional wind bias, the opposite direction of the LLJ (Fig. 8b). Because it cannot be expected for the LLJ to be present at 700 hPa in North America, 850-hPa error is also analyzed (Figs. 8c,d). There was much less dry bias at 850 hPa relative to 700 hPa in both continents. The spatial distribution of equatorward wind biases was similar between levels, however. Furthermore, the LLJ in both continents tends to maximize overnight (Bonner 1968; Vera et al. 2006) and thus 0000 UTC verification likely does not capture error directly from the LLJ. However, its indirect influence in either continent cannot be ruled out, as LLJ presence in the model (or lack thereof) could cause future convective forecast errors evident at both pressure levels. Though not addressed in this study, convective scale errors imposed by the SALLJ would serve as an interesting route for future work.

Meridional wind bias can result from an inaccurate forecast of both strength and/or direction; thus, we break down the forecasted and observed meridional wind values that compose the monthly means for two key cities in each continent (Fig. 9). In Córdoba (Fig. 9a), forecasts were too strong upon observed equatorward wind (opposing SALLJ) and were too weak upon observed poleward wind (with SALLJ). Both of these model errors contribute to the mean bias of 2.8 m s^{-1} in Fig. 8a. Alternatively in Mendoza, forecasts missed weak equatorward wind observations and slightly over-forecasted the poleward component (Fig. 9b). Both Dallas, Texas, and Springfield, Missouri, featured nearly equal and opposite trends as Córdoba, with weak poleward and strong equatorward forecasts (Figs. 9c,d), contributing to the −2.53 and −2.06 m s^{-1} errors, respectively. In general, it is clear that under-forecasts of poleward wind speed largely contribute to the overall biases in each continent.

5. South and North American cases

As described in section 1 within the context of previous work, we hypothesized that model error maximizes in association with widespread convection. With this in mind, we identify times of relatively high error and check for the presence of convection, or alternatively, assess the error on days in which a large MCS was present over subtropical South America. Daily mean, as opposed to monthly mean 0000 UTC RH RMSE values (as in Fig. 7), not only allows for further comparison between continents, but it also highlights specific instances of error (Fig. 10). As previously noted, RMSE in South America tended to be greater, but also varied much more, likely due to the fewer sounding locations considered. The date 22 December 2018 stands out as a clear maximum, with GF and KF exceeding an average of 40% and 30% error, respectively (Fig. 10a). Below we diagnose the error from this day in addition to that of a widespread back-building and upstream propagating MCS case that took place on 11 November 2018. Afterward we discuss the North America maximum and

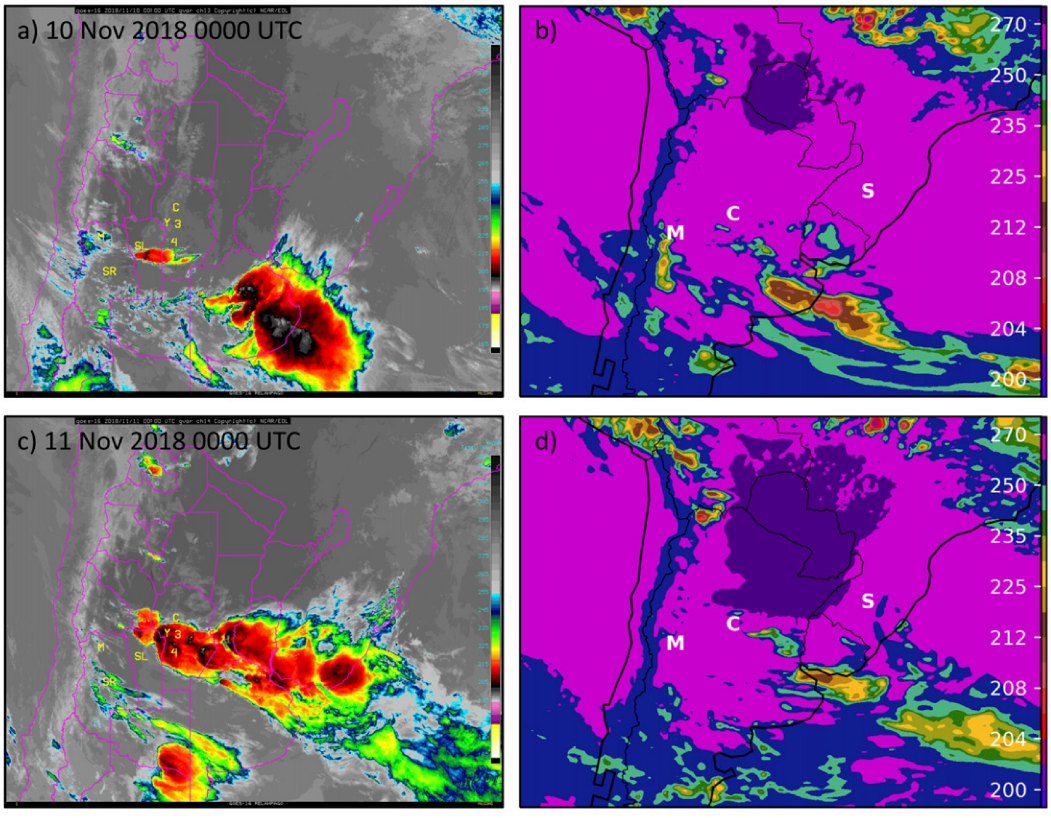

FIG. 13. (left) Observed (via *GOES-16*) and (right) forecasted (24-h lead; WRF with GF) IR temperature (K) for (a),(b) 0000 UTC 10 Nov and (c),(d) 0000 UTC 11 Nov 2018. M, C, and S on the simulated plots indicate locations of Mendoza, Córdoba, and Santa Maria cities, respectively. More local landmarks are also marked in (a) and (c): SR, San Rafael; SL, San Luis; Y, Villa Yacanto; 3, Río Tercero; and 4, Río Cuarto.

minimum error days on 17 May and 5 May, respectively (Fig. 10b).

a. *South America cases: 22 December and 10–11 November 2018*

The date 22 December 2018 featured widespread convection primarily north of 25°S, Argentina, and Uruguay (Fig. 11a). On this day, there were some very large positive RH errors in the forecasts in addition to the negative RH errors that were more commonly observed. The largest RH error of +75% occurred at Santa Maria, BR, just south of the convective feature (Fig. 11c). This extreme wet bias in the 24-h GF forecast can be explained by identifying that the model forecast inaccurately predicted this convective band to extend further south and thus rain over Santa Maria (Fig. 11b).

There was also a very large discrepancy between forecasted and observed meridional wind at Santa Maria and surrounding locations. The "observed" 48-h backward parcel trajectories ending at 700 hPa around Santa Maria, as visualized using GDAS 1° reanalysis and the HYSPLIT model tool, suggest nearly zonal flow approaching the region (blue tracks in Fig. 11d). The trajectory ending at Santa Maria actually extends back to the Andes and likely carried dry air as a result (middle blue track in Fig. 11d). The model forecast on the other hand had a strong poleward bias of between 2.17 and 5.28 m s^{-1} for locations north of Uruguay (Fig. 11c). This poleward direction seems to truly occur farther north where convection actually took place (green tracks in Fig. 11d), further alluding to the model misplacement of convection. Figure 12 compares the observed and 24-h GF forecasted soundings from this time and location. While the temperature profiles are similar, the forecasted 600–700-hPa layer is much more moist, featuring a 700-hPa dewpoint temperature of 7.8°C where −20°C was observed. It is also interesting that the forecasted low levels feature moisture and southerly flow as convection occurred to the north, but this is out of the scope of the current study.

While it appears that the main source of both RH and meridional wind error on this day is due to the inaccurate forecast of the convection location, another likely factor is the lack of stations operating in Argentina, namely Córdoba and Mendoza (Fig. 11c). This region was clear of any weather and likely would have reduced the mean error if data were available.

One of the more fascinating events during RELAMPAGO initiated around 0000 UTC 10 November 2018 (Fig. 13a), featured rapid back-building convection that grew upscale east of the SDC within 24 h (Fig. 13c), and later spawned multiple

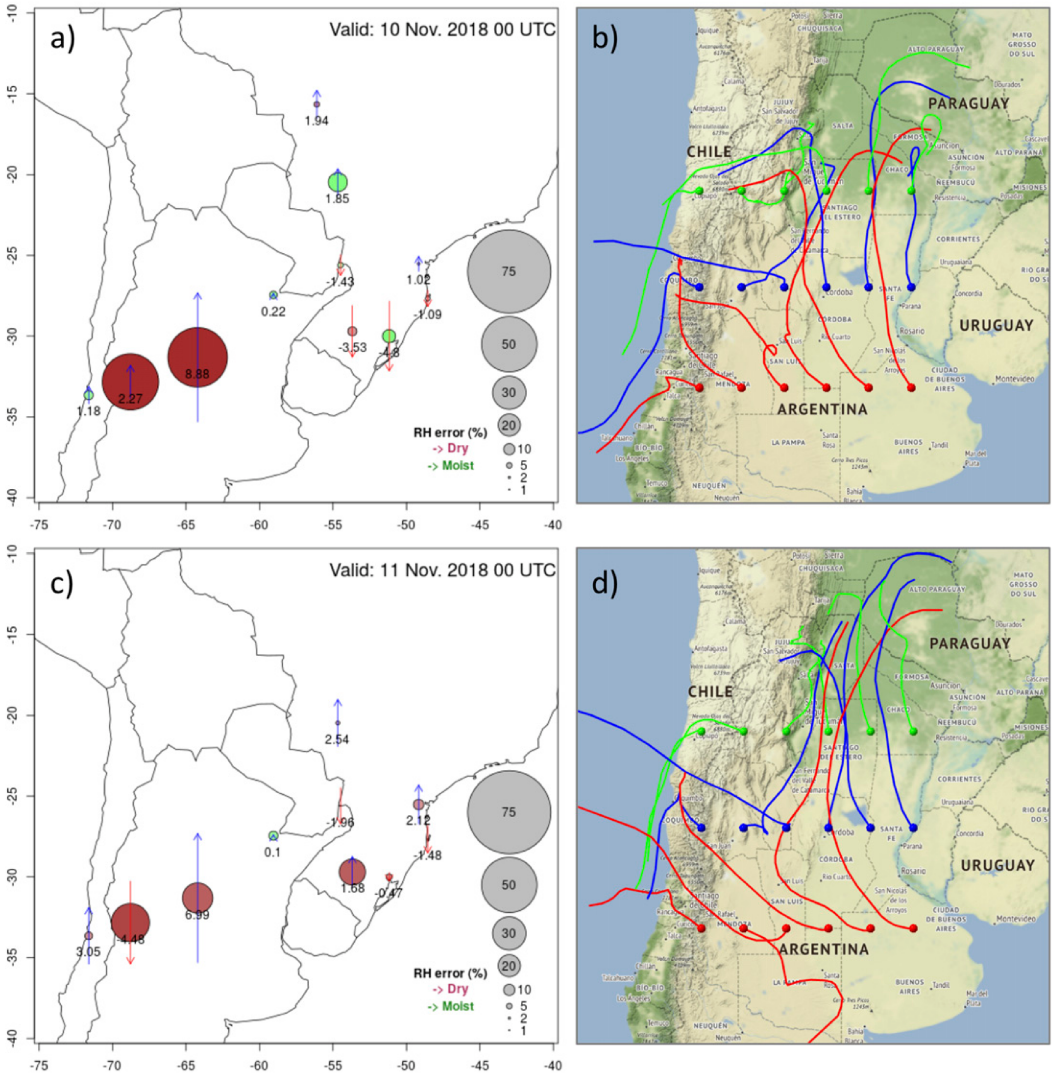

FIG. 14. The 700-hPa RH and meridional wind 24-h forecast bias as in Fig. 11c, but for (a) 10 and (c) 11 Nov, and GDAS 1° reanalysis 48-h backward trajectories ending at 700 hPa at 0000 UTC (b) 10 and (d) 11 Nov via NOAA HYSPLIT model.

isolated supercells. As a perfect example of South America convective initiation (Rasmussen and Houze 2016) and upstream propagation (Anabor et al. 2008), this large MCS combined the roles of an extremely deep, slow-moving synoptic trough impinging upon western Chile, lee cyclogenesis, and southward moisture advection along the high terrain (Piersante et al. 2021).

Though the convection during this case was widespread spatially and temporally, the average RMSE at 0000 UTC 10 November was about 25% for both CPs and even smaller on 11 November (Fig. 10a). The bulk of this error was in Córdoba and Mendoza, with dry biases around 50% and 30% on 10 and 11 November, respectively (Figs. 14a,c). Both locations also featured a strong equatorward meridional wind bias on 10 November, opposing the SALLJ and likely partially explaining the dry bias (Fig. 14a). The reanalysis Córdoba backward trajectory shows northeastward subsidence from the Andes followed by southward flow likely associated with the SALLJ. Mendoza, located in the immediate foothills of the high terrain, primarily features southeastward subsidence (Fig. 14b). The 24-h WRF forecast trajectories of parcels ending at 700 hPa near Mendoza and Córdoba also featured subsiding flow from the western terrain (Fig. 15a). However, the forecast trajectories ending near Córdoba lacked the northerly component featured in the reanalysis, which likely influenced the moisture forecast error. GF and KF trajectories ending near Mendoza were nearly identical while there was more disagreement within GF and KF trajectories in the vicinity of the Sierras de Córdoba, further alluding to the complexities of forecasting near this small mountain range.

These trends persisted in Córdoba through 11 November while the Mendoza meridional wind bias shifted poleward

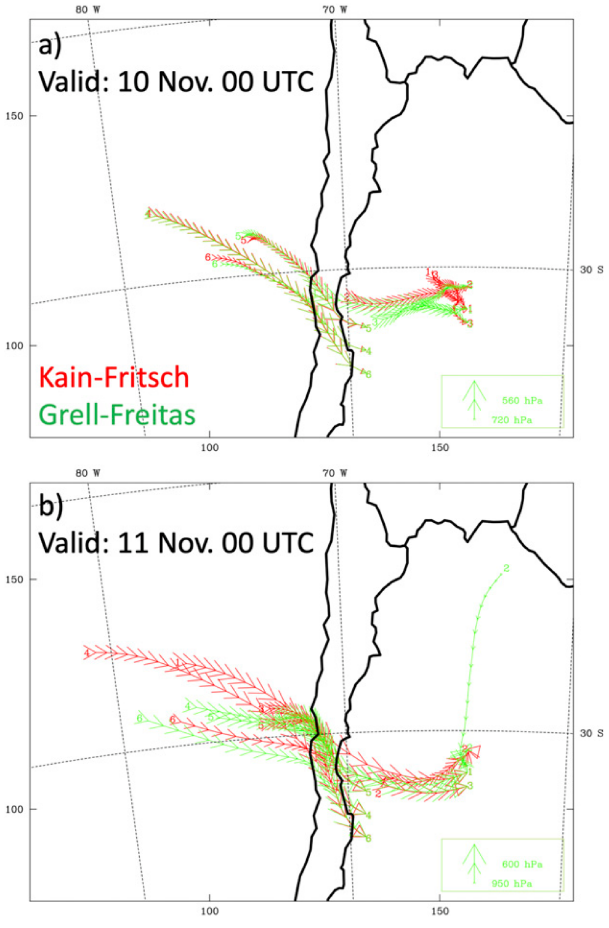

FIG. 15. The 24-h backward trajectories ending at 700 hPa near Córdoba (1–3) and Mendoza (4–6) from WRF forecasts valid at (a) 0000 UTC 10 Nov and (b) 0000 UTC 11 Nov 2018. Trajectories labeled 1 and 4 indicate parcel paths ending over Córdoba and Mendoza, respectively. Wider arrows along each path indicates lower pressure (higher in atmosphere), and color indicates the corresponding CP used in WRF. These backward trajectories were calculated and plotted via RIP (http://www2.mmm.ucar.edu/wrf/users/docs/ripug.htm) from the preexisting WRF output files.

(Fig. 14c) and featured a northwesterly backward trajectory via reanalysis (Fig. 14d). The forecasts of these trajectories on the other hand all continued to feature westerly subsidence, with the exception of one trajectory ending north of Córdoba, which was northerly as in the reanalysis (Fig. 15b). Thus, there was a discrepancy between the Mendoza forecast and reanalysis trajectory with regard to the parcel origin. An inaccurate timing of the passage of the low pressure system within the model likely causes this shift in bias, as the eastward passage of such a system causes a wind shift in Argentina (Rasmussen and Houze 2016).

The depth of the SALLJ is evident within the 0000 UTC 10 November Córdoba sounding, as a strong northerly wind component persisted through 700 hPa (Fig. 16a). The 24-h Córdoba forecast sounding on the other hand failed to represent such a depth, extending the northerly component to only about 750 hPa (Fig. 16b). Like this forecast sounding, the forecasted parcel trajectory valid at this time also shows primarily easterly flow at 700 hPa over Córdoba (Fig. 15a). The observed and forecasted meridional wind values were approximately -8.1 and $0\,\mathrm{m\,s^{-1}}$, respectively, leading to the bias shown in Fig. 14a. The thermodynamic forecast at this level was warm and dry, with temperature and dewpoint temperature at 10.8° and −3.5°C instead of 8.4° and 7.2°C, explaining the dry RH bias in Fig. 14a. While there is much more to compare between the forecasted and observed soundings, such as the differences in CAPE, MUCAPE, and CIN, this is beyond the scope of this study and should be an interesting area for future work.

In summary, the limited data of this region suggest that the model struggled to accurately represent subsidence from the Andes in addition to the strength of the SALLJ at 700 hPa before and after initiation, both of which seem to contribute to the dry 24-h forecast bias at 700 hPa. Given that the model forecast did not capture the widespread upscale growth and back-building features of this MCS (Figs. 13b,d), the mean error for these days would likely be even greater had there been more operational soundings to verify against near these features.

b. *North America cases: 17 May and 5 May 2016*

The cases at 0000 UTC 17 May and 5 May featured the greatest and least average error among North America stations during the 2016 warm season, respectively (Fig. 10b). The CONUS NEXRAD radar mosaic on 17 May 2016 reveals discontinuous MCSs across the central United States, a convective line through the Great Lakes region, and some convection in LA and FL (Fig. 17a). The date 5 May 2016 on the other hand was rather clear of storm activity in the central United States, but featured convection in FL in addition to some stratiform rain associated with a comma-shaped system in the eastern United States (Fig. 17c). The GF model 24-h forecast did a reasonable job depicting the location and intensity of these storms on both days (Figs. 17b,d).

Robust dry biases greater than or equal to 50% on 17 May occurred near the convection mentioned above, namely Kansas/Oklahoma, Wisconsin, and Florida (Fig. 18a). Various wet biases were also present, some due to model misplacement of storms. Unlike central Argentina, there was mainly a poleward meridional wind bias throughout the central United States (Fig. 18a). While "observed" backward trajectories within this region featured a partial northward component, the flow primarily subsided from the high terrain in the west as in South America (Fig. 19a).

Both RH and meridional wind biases at 700 hPa in the central United States on 5 May were substantially smaller (Fig. 18b). Additionally, the flow was uniformly southward, avoiding any interaction with the Rockies to the west (Fig. 19b), and yielding a relatively straightforward 24-h forecast.

This comparison between South and North America error days in the context of the four cases presented herein suggests that errors in both continents occur when there is flow from over the western mountainous terrain and large convective systems to the east. Previous work explains this flow by the

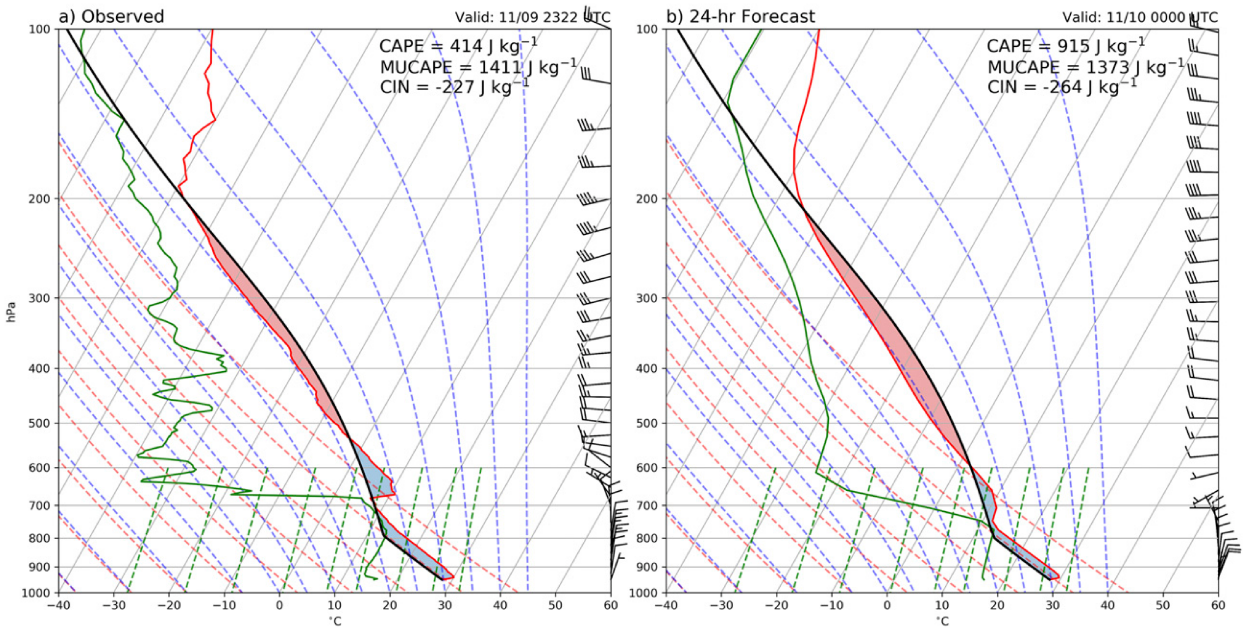

FIG. 16. (a) Observed and (b) Grell–Freitas forecasted Córdoba soundings valid at 0000 UTC 10 Nov 2018. Pressure (hPa) and temperature (°C) serve as the vertical and horizontal coordinates, respectively. Wind barbs on the right of each skew *T*–log*p* diagram indicate direction and speed, where a long tick represents 10 m s^{-1} and a short tick represents 5 m s^{-1}. Temperature (dewpoint temperature) is plotted in red (green) and the parcel path in black; areas of CAPE (CIN) are shaded in red (blue). Values of CAPE, MUCAPE, and CIN are shown in the upper-right corner. Moist adiabats, dry adiabats, and mixing lines are represented by dashed lines of blue, red, and green, respectively.

placement of an upper-level trough over the mountains; EMLs, a capping inversion, and a LLJ along the terrain can occur in tandem as this impinging trough initiates lee cyclogenesis, acting to initiate and strengthen MCS-like systems east of the high terrain (Carlson et al. 1983; Rasmussen and Houze 2011, 2016; Ribeiro and Bosart 2018). Once widespread convection is present, additional error can quickly result due to model misplacement of the storms. However, the cases in this study most notably show that the locations experiencing relatively large thermodynamic error are associated with westerly subsidence. Additionally, these cases suggest that poor model representation of convective storms in the vicinity of these errors likely indirectly impact nearby thermodynamic forecasts. Because westerly subsidence is linked to thermodynamic errors and convective initiation, model representation of westerly air descending from mountainous terrain must be improved. The ongoing challenge facing the improvement of NWP in subtropical South America is the lack of a long-term, widespread, and continuous observation network.

6. Summary and conclusions

In the first part of this study, we verify precipitation forecasts over CONUS from 19 deterministic WRF Model configurations with 20-km horizontal resolution against NCEP Stage-IV analyses to arrive at three key findings: 1) precipitation forecast skill is greatest during the cool season, 2) skill decreases with increasing precipitation amounts, and 3) simulations using the same CP have similar skill throughout the year, but most notably during the warm season when more convection occurs. Depending on the application, one could sacrifice skill at one time or precipitation threshold to be more accurate at another. This work highlights specific biases among common CPs to guide this sort of decision making within the NWP community.

While previous work suggests that CP also influences precipitation skill in South America using reanalysis data (Blázquez and Nuñez 2009), there is still room for further NWP exploration within this region given the significant impact of extreme rainfall and model error in South America. For example, it would be interesting to compare our North America results to a similar ensemble-based precipitation bias analysis, perhaps employing NASA's Global Precipitation Measurement mission IMERG precipitation data in South America in lieu of Stage-IV analyses.

With these results in mind, the second part of this study consists of verifying the forecasted thermodynamic environments against observational sounding networks in North and South America, employing two WRF configurations with different CPs. Both continents featured a clear and persistent midlevel dry model bias, particularly at 700 hPa, throughout their respective warm seasons. Large bias occurred in association with westerly flow from the mountainous terrain and large MCS-like systems in the eastern plains. Accurately forecasting flow over mountains in addition to convective initiation and placement of the resulting storms is very challenging, all likely contributing to the error we see in this current study.

Error in South America was consistently greater. The lack of widespread observation stations is a plausible factor in this; fewer points of verification reduce confidence in the mean

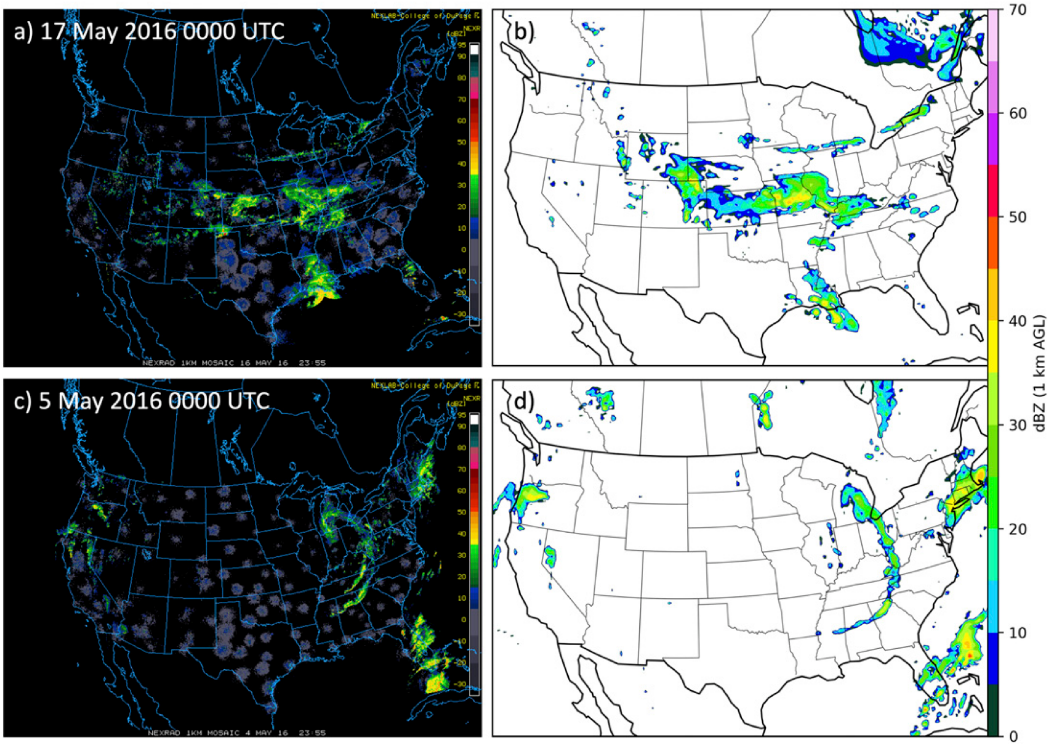

FIG. 17. Observed 1-km radar reflectivity (dBZ) via NEXRAD at 0000 UTC (a) 17 and (c) 5 May vs 24-h forecasted 1-km radar reflectivity for 0000 UTC (b) 17 May and (d) 5 May 2016.

error and also limit the data assimilation into the model to improve forecasts. There are few to no stations in and west of the Andes Mountains, while there is an abundance within the Rocky Mountains and the western CONUS.

Furthermore, even models with 20-km grid spacing seem to struggle to capture the complex topography of the Andes. The significant height and narrow mountain profile of the Andes allows for a deeper northerly LLJ, often funneled along the high terrain (Insel et al. 2010; Rasmussen and Houze 2016). The Andean foothills and the SDC frequently trigger and terrain-tie convection (Rasmussen and Houze 2011, 2016), which the WRF Model forecast inadequately represented for a

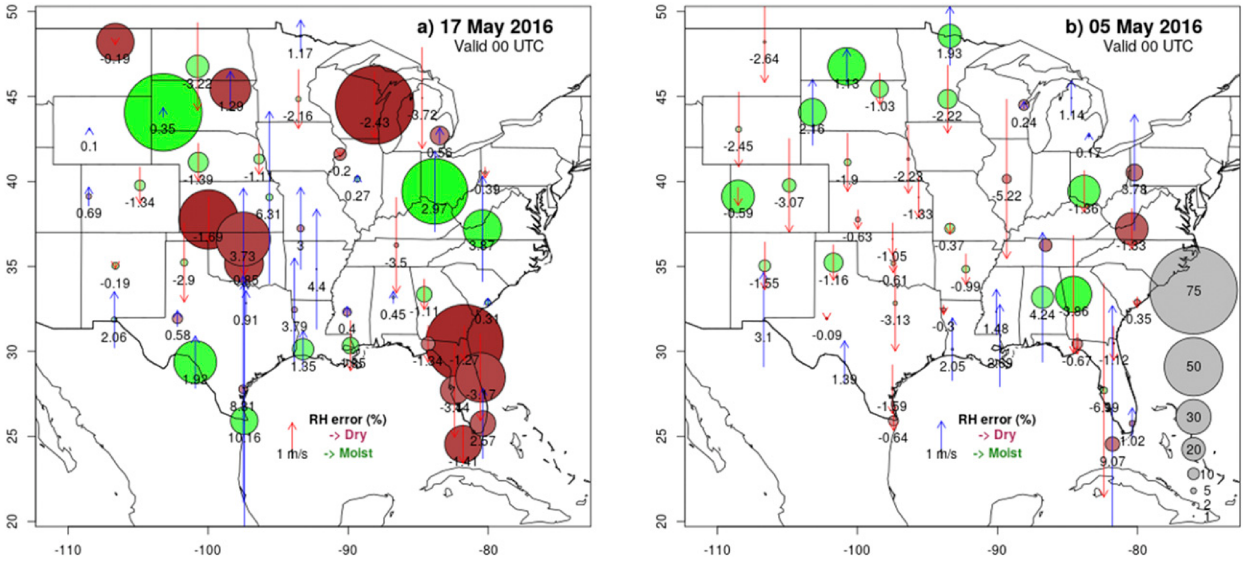

FIG. 18. As in Figs. 14a and 14c, but for (a) 17 and (b) 5 May 2016 over North America.

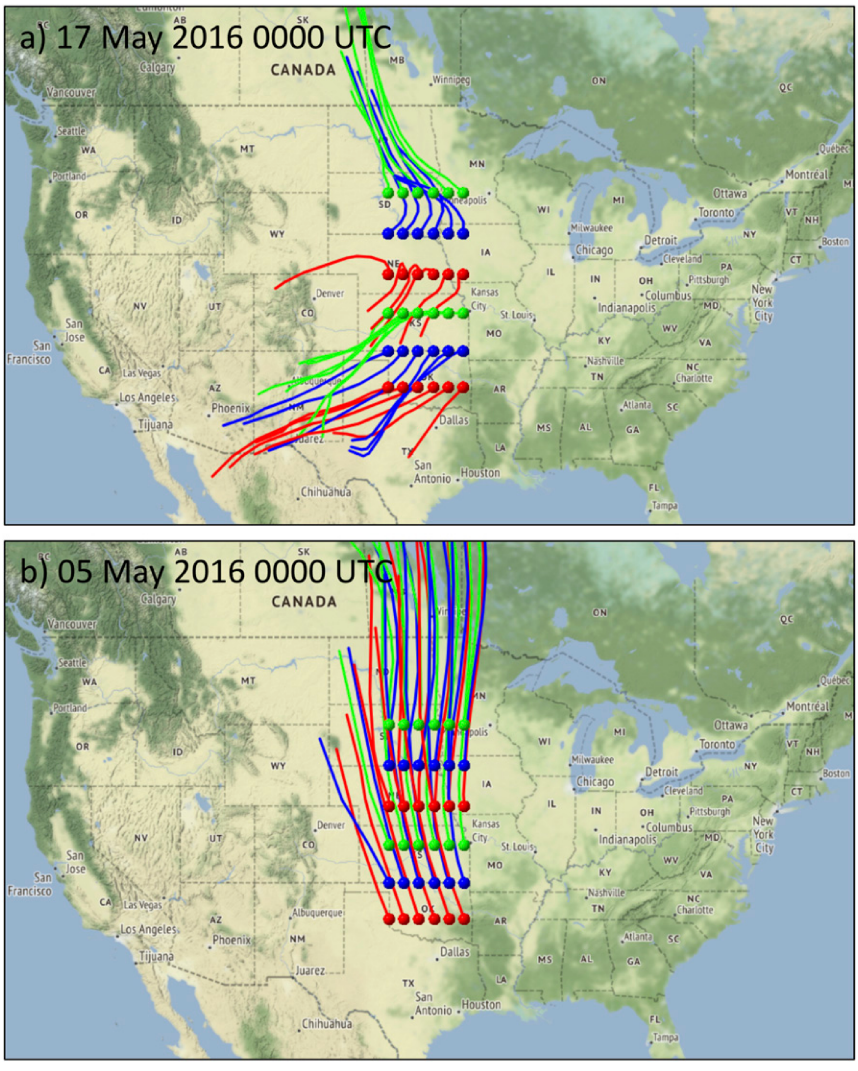

FIG. 19. GDAS 1° reanalysis 48-h backward trajectories ending at 700 hPa on (a) 17 and (b) 5 May 2016 via NOAA HYSPLIT model. Colors indicate latitudes of endpoints.

large, upscale-growing MCS case that occurred during RELAMPAGO. We show that the forecast prior to its convective initiation near the SDC failed to capture the moisture and northerly wind speeds at 700 hPa. With North America cases on the other hand, it appears the midlevel moisture error was more related to subsidence than LLJ. Thus, it is likely that the model representation of the depth of the SALLJ and the complex topography causes additional errors in South America. Future work could run even finer, convection-permitting resolutions in South America to pinpoint the role of terrain smoothing and parameterized convection in these forecast biases.

Fortunately today it is much more reasonable to forecast weather at convection-permitting resolution and therefore many of the issues we raise here may likely be resolved. However, regional and global climate models usually still rely on CPs. Considering the growing importance of understanding convective storms in a future climate, supplemental work should also look into CP bias correction among these larger-scale models, particularly in regard to connecting specific physical processes to model biases. The relation between moisture and precipitation errors could serve as a proper starting point. Furthermore, global models such as GFS and ECMWF likely carry their own biases that manifest when serving as parent models for WRF simulations. To attribute errors to parent models in the context of this continental comparison, an additional study should force WRF simulations to those analyzed herein with a range of global model forecast output. Caron and Steenburgh (2020) have highlighted differences in western CONUS cool-season precipitation skill score between GFS (versions 15.0 and 14.0) and high-resolution ECMWF Integrated Forecasting System. A similar warm-season comparison between North and South America would be a natural supplement to the current study, though a

multinetwork precipitation observation dataset is needed in South America.

Both North and South America are home to some of the deepest convection on the planet, spawning various forms of severe weather that threaten the economic and social welfare of many. As a result, understanding and improving prediction of the thermodynamic environments supporting organized convection is critical for limiting damage today and in a future climate. The impact of large mountain ranges, such as the Rockies and Andes, on weather downstream has been widely studied for decades. However, with the steady advancement of NWP in addition to observational datasets via field campaigns such as RELAMPAGO, we are increasingly able to explain the impacts of terrain and subtle differences in severe weather phenomena between regions of the world. This study in particular suggests that model error comes from similar processes in both North and South America, though certain characteristics of the Andes in contrast with the Rocky Mountains forces models to struggle more in South America. Looking ahead, we hope this work continues the trend of comparing localized severe weather across various regions with similar large-scale environments by taking advantage of advances in technology and global collaboration to obtain ground observations via field campaigns.

Acknowledgments. Thank you to Scot Loehrer for providing a crucial *GOES-16* infrared temperature image. The authors thank the Big Weather Web ensemble research and development team, and in particular Kevin Tyle (University at Albany) and Gretchen Mullendore (University of North Dakota) for assistance in accessing and analyzing the output. Last, the authors thank the three anonymous reviewers whose suggestions helped greatly improve this manuscript. Stage-IV analyses data were provided via the National Center for Atmospheric Research (NCAR). Global operational radiosonde data were provided by the National Oceanic and Atmospheric Administration (NOAA). This research was supported by NSF Grants ACI-1450089, AGS-1661657, and AGS-1661862.

Data availability statement. Big Weather Web WRF ensemble members over North America are available at http://149.165.157.204/thredds/catalog.html. South America WRF output is stored on a CSU server and is available upon request. NCEP Stage-IV analyses were accessed through the Earth Observing Laboratory (https://data.eol.ucar.edu/dataset/21.093). North and South America soundings were accessed through the Research Data Archive (https://rda.ucar.edu/datasets/ds351.0/) and the RELAMPAGO Data Archive (https://data.eol.ucar.edu/master_lists/generated/relampago/), respectively. NEXRAD archive radar imagery was accessed online via the Mesoscale and Microscale Meteorology Laboratory of NCAR (http://www2.mmm.ucar.edu/imagearchive/).

REFERENCES

Anabor, V., D. J. Stensrud, and O. L. de Moraes, 2008: Serial upstream-propagating mesoscale convective system events over southeastern South America. *Mon. Wea. Rev.*, **136**, 3087–3105, https://doi.org/10.1175/2007MWR2334.1.

Blázquez, J., and M. N. Nuñez, 2009: Sensitivity to convective parameterization in the WRF regional model in southern South America. *Ninth Int. Conf. on Southern Hemisphere Meteorology and Oceanography*, Melbourne, Australia, Australian Meteorological and Oceanographic Society, 1–6.

Bonner, W. D., 1968: Climatology of the low-level jet. *Mon. Wea. Rev.*, **96**, 833–850, https://doi.org/10.1175/1520-0493(1968)096<0833:COTLLJ>2.0.CO;2.

Bryan, G. H., J. C. Wyngaard, and J. M. Fritsch, 2003: Resolution requirements for the simulation of deep moist convection. *Mon. Wea. Rev.*, **131**, 2394–2416, https://doi.org/10.1175/1520-0493(2003)131<2394:RRFTSO>2.0.CO;2.

Carlson, T. N., S. G. Benjamin, G. S. Forbes, and Y.-F. Li, 1983: Elevated mixed layers in the regional severe storm environment: Conceptual model and case studies. *Mon. Wea. Rev.*, **111**, 1453–1474, https://doi.org/10.1175/1520-0493(1983)111<1453:EMLITR>2.0.CO;2.

Caron, M., and W. J. Steenburgh, 2020: Evaluation of recent NCEP operational model upgrades for cool-season precipitation forecasting over the western conterminous United States. *Wea. Forecasting*, **35**, 857–877, https://doi.org/10.1175/WAF-D-19-0182.1.

Cecil, D. J., and C. B. Blankenship, 2012: Toward a global climatology of severe hailstorms as estimated by satellite passive microwave imagers. *J. Climate*, **25**, 687–703, https://doi.org/10.1175/JCLI-D-11-00130.1.

Clark, A. J., W. A. Gallus Jr., and T.-C. Chen, 2007: Comparison of the diurnal precipitation cycle in convection-resolving and non-convection-resolving mesoscale models. *Mon. Wea. Rev.*, **135**, 3456–3473, https://doi.org/10.1175/MWR3467.1.

——, ——, M. Xue, and F. Kong, 2009: A comparison of precipitation forecast skill between small convection-allowing and large convection-parameterizing ensembles. *Wea. Forecasting*, **24**, 1121–1140, https://doi.org/10.1175/2009WAF2222222.1.

——, and Coauthors, 2012: An overview of the 2010 Hazardous Weather Testbed Experimental Forecast Program Spring Experiment. *Bull. Amer. Meteor. Soc.*, **93**, 55–74, https://doi.org/10.1175/BAMS-D-11-00040.1.

——, and Coauthors, 2018: The Community Leveraged Unified Ensemble (CLUE) in the 2016 NOAA/Hazardous Weather Testbed Spring Forecasting Experiment. *Bull. Amer. Meteor. Soc.*, **99**, 1433–1448, https://doi.org/10.1175/BAMS-D-16-0309.1.

Cordeira, J. M., N. D. Metz, M. E. Howarth, and T. J. Galarneau Jr., 2017: Multiscale upstream and in situ precursors to the elevated mixed layer and high-impact weather over the Midwest United States. *Wea. Forecasting*, **32**, 905–923, https://doi.org/10.1175/WAF-D-16-0122.1.

Davis, C. A., K. W. Manning, R. E. Carbone, S. B. Trier, and J. D. Tuttle, 2003: Coherence of warm-season continental rainfall in numerical weather prediction models. *Mon. Wea. Rev.*, **131**, 2667–2679, https://doi.org/10.1175/1520-0493(2003)131<2667:COWCRI>2.0.CO;2.

Durkee, J. D., T. L. Mote, and J. M. Shepherd, 2009: The contribution of mesoscale convective complexes into rainfall across subtropical South America. *J. Climate*, **22**, 4590–4605, https://doi.org/10.1175/2009JCLI2858.1.

Fritsch, J. M., R. J. Kane, and C. R. Chelius, 1986: The contribution of mesoscale convective weather systems to the warm-season precipitation in the United States. *J. Climate Appl. Meteor.*, **25**, 1333–1345, https://doi.org/10.1175/1520-0450(1986)025<1333:TCOMCW>2.0.CO;2.

Gotway, J. H., and Coauthors, 2018: Model evaluation tools version 8.0 (METv8.0) user's guide. Developemental Testbed

Center, Boulder, CO, 432 pp., https://dtcenter.org/sites/default/files/community-code/met/docs/user-guide/MET_Users_Guide_v8.0.pdf.

Grell, G. A., and S. R. Freitas, 2014: A scale and aerosol aware stochastic convective parameterization for weather and air quality modeling. *Atmos. Chem. Phys.*, **14**, 5233–5250, https://doi.org/10.5194/acp-14-5233-2014.

Grenier, H., and C. S. Bretherton, 2001: A moist PBL parameterization for large-scale models and its application to subtropical cloud-topped marine boundary layers. *Mon. Wea. Rev.*, **129**, 357–377, https://doi.org/10.1175/1520-0493(2001)129<0357:AMPPFL>2.0.CO;2.

Haberlie, A. M., and W. S. Ashley, 2019: A radar-based climatology of mesoscale convective systems in the United States. *J. Climate*, **32**, 1591–1606, https://doi.org/10.1175/JCLI-D-18-0559.1.

Hodges, D., and Z. Pu, 2019: Characteristics and variations of low-level jets and environmental factors associated with summer precipitation extremes over the Great Plains. *J. Climate*, **32**, 5123–5144, https://doi.org/10.1175/JCLI-D-18-0553.1.

Hong, S.-Y., and J.-O. J. Lim, 2006: The WRF single-moment 6-class microphysics scheme (WSM6). *J. Korean Meteor. Soc.*, **42**, 129–151.

——, Y. Noh, and J. Dudhia, 2006: A new vertical diffusion package with an explicit treatment of entrainment processes. *Mon. Wea. Rev.*, **134**, 2318–2341, https://doi.org/10.1175/MWR3199.1.

Houze, R. A., Jr., 2004: Mesoscale convective systems. *Rev. Geophys.*, **42**, RG4003, https://doi.org/10.1029/2004RG000150.

——, K. L. Rasmussen, M. D. Zuluaga, and S. R. Brodzik, 2015: The variable nature of convection in the tropics and subtropics: A legacy of 16 years of the Tropical Rainfall Measuring Mission satellite. *Rev. Geophys.*, **53**, 994–1021, https://doi.org/10.1002/2015RG000488.

Iacono, M. J., J. S. Delamere, E. J. Mlawer, M. W. Shephard, S. A. Clough, and W. D. Collins, 2008: Radiative forcing by long-lived greenhouse gases: Calculations with the AER radiative transfer models. *J. Geophys. Res.*, **113**, D13103, https://doi.org/10.1029/2008JD009944.

Insel, N., C. J. Poulsen, and T. A. Ehlers, 2010: Influence of the Andes Mountains on South American moisture transport, convection, and precipitation. *Climate Dyn.*, **35**, 1477–1492, https://doi.org/10.1007/s00382-009-0637-1.

Iyer, E. R., A. J. Clark, M. Xue, and F. Kong, 2016: A comparison of 36–60-h precipitation forecasts from convection-allowing and convection-parameterizing ensembles. *Wea. Forecasting*, **31**, 647–661, https://doi.org/10.1175/WAF-D-15-0143.1.

Janjić, Z. I., 1994: The step-mountain eta coordinate model: Further developments of the convection, viscous sublayer, and turbulence closure schemes. *Mon. Wea. Rev.*, **122**, 927–945, https://doi.org/10.1175/1520-0493(1994)122<0927:TSMECM>2.0.CO;2.

Jankov, I., W. A. Gallus, M. Segal, B. Shaw, and S. E. Koch, 2005: The impact of different WRF Model physical parameterizations and their interactions on warm season MCS rainfall. *Wea. Forecasting*, **20**, 1048–1060, https://doi.org/10.1175/WAF888.1.

Jeworrek, J., G. West, and R. Stull, 2019: Evaluation of cumulus and microphysics parameterizations in WRF across the convective gray zone. *Wea. Forecasting*, **34**, 1097–1115, https://doi.org/10.1175/WAF-D-18-0178.1.

Kain, J. S., 2004: The Kain–Fritsch convective parameterization: An update. *J. Appl. Meteor.*, **43**, 170–181, https://doi.org/10.1175/1520-0450(2004)043<0170:TKCPAU>2.0.CO;2.

Laing, A. G., and J. G. Fritsch, 1997: The global population of mesoscale convective complexes. *Quart. J. Roy. Meteor. Soc.*, **123**, 389–405, https://doi.org/10.1002/qj.49712353807.

Liang, X.-Z., and Coauthors, 2012: Regional climate–weather research and forecasting model. *Bull. Amer. Meteor. Soc.*, **93**, 1363–1387, https://doi.org/10.1175/BAMS-D-11-00180.1.

Lin, Y., and K. E. Mitchell, 2005: The NCEP Stage II/IV hourly precipitation analyses: Development and applications. *19th Conf. on Hydrology*, San Diego, CA, Amer. Meteor. Soc., 1.2, https://ams.confex.com/ams/Annual2005/techprogram/paper_83847.htm.

Liu, C., M. W. Moncrieff, J. D. Tuttle, and R. E. Carbone, 2006: Explicit and parameterized episodes of warm-season precipitation over the continental United States. *Adv. Atmos. Sci.*, **23**, 91–105, https://doi.org/10.1007/s00376-006-0010-9.

Maddox, R. A., 1980: Mesoscale convective complexes. *Bull. Amer. Meteor. Soc.*, **61**, 1374–1387, https://doi.org/10.1175/1520-0477(1980)061<1374:MCC>2.0.CO;2.

——, 1983: Large-scale meteorological conditions associated with midlatitude, mesoscale convective complexes. *Mon. Wea. Rev.*, **111**, 1475–1493, https://doi.org/10.1175/1520-0493(1983)111<1475:LSMCAW>2.0.CO;2.

Maltzahn, C., and Coauthors, 2016: Big Weather Web: A common and sustainable big data infrastructure in support of weather prediction research and education in universities. Accessed 1 June 2019, http://bigweatherweb.org.

Marengo, J. A., M. W. Douglas, and P. L. Silva Dias, 2002: The South American low level jet east of the Andes during the 1999 LBATRMM and LBA-WET AMC campaign. *J. Geophys. Res.*, **107**, 8079, https://doi.org/10.1029/2001JD001188.

——, W. R. Soares, C. Saulo, and M. Nicolini, 2004: Climatology of the low-level jet east of the Andes as derived from the NCEP–NCAR reanalyses: Characteristics and temporal variability. *J. Climate*, **17**, 2261–2280, https://doi.org/10.1175/1520-0442(2004)017<2261:COTLJE>2.0.CO;2.

Milbrandt, J. A., and M. K. Yau, 2005: A multimoment bulk microphysics parameterization. Part I: Analysis of the role of the spectral shape parameter. *J. Atmos. Sci.*, **62**, 3051–3064, https://doi.org/10.1175/JAS3534.1.

Morrison, H., G. Thompson, and V. Tatarskii, 2009: Impact of cloud microphysics on the development of trailing stratiform precipitation in a simulated squall line: Comparison of one- and two-moment schemes. *Mon. Wea. Rev.*, **137**, 991–1007, https://doi.org/10.1175/2008MWR2556.1.

Müller, O. V., M. A. Lovino, and E. H. Berbery, 2016: Evaluation of WRF Model forecasts and their use for hydroclimate monitoring over southern South America. *Wea. Forecasting*, **31**, 1001–1017, https://doi.org/10.1175/WAF-D-15-0130.1.

Nakanishi, M., and H. Niino, 2009: Development of an improved turbulence closure model for the atmospheric boundary layer. *J. Meteor. Soc. Japan*, **87**, 895–912, https://doi.org/10.2151/jmsj.87.895.

Nascimento, M. G., D. L. Herdies, and D. O. Souza, 2016: The South American water balance: The influence of low-level jets. *J. Climate*, **29**, 1429–1449, https://doi.org/10.1175/JCLI-D-15-0065.1.

Nesbitt, S. W., R. Cifelli, and S. A. Rutledge, 2006: Storm morphology and rainfall characteristics of TRMM precipitation features. *Mon. Wea. Rev.*, **134**, 2702–2721, https://doi.org/10.1175/MWR3200.1.

——, and Coauthors, 2021: A storm safari in subtropical South America: Proyecto RELAMPAGO. *Bull. Amer. Meteor. Soc.*, https://doi.org/10.1175/BAMS-D-20-0029.1, in press.

Oliveira, M. I., E. L. Nascimento, and C. Kannenberg, 2018: A new look at the identification of low-level jets in South America. *Mon. Wea. Rev.*, **146**, 2315–2334, https://doi.org/10.1175/MWR-D-17-0237.1.

Petch, J., 2006: Sensitivity studies of developing convection in a cloud-resolving model. *Quart. J. Roy. Meteor. Soc.*, **132**, 345–358, https://doi.org/10.1256/qj.05.71.

Piersante, J. O., K. Rasmussen, R. S. Schumacher, A. K. Rowe, and L. A. McMurdie, 2021: A synoptic evolution comparison of the smallest and largest MCSs in subtropical South America between spring and summer. *Mon. Wea. Rev.*, https://doi.org/10.1175/MWR-D-20-0208.1, in press.

Pleim, J. E., 2007: A combined local and nonlocal closure model for the atmospheric boundary layer. Part I: Model description and testing. *J. Appl. Meteor. Climatol.*, **46**, 1383–1395, https://doi.org/10.1175/JAM2539.1.

Porter, J. M., L. L. Means, J. E. Hovde, and W. B. Chappell, 1955: A synoptic study on the formation of squall lines in the north central United States. *Bull. Amer. Meteor. Soc.*, **36**, 390–396, https://doi.org/10.1175/1520-0477-36.8.390.

Rasmussen, K. L., and R. A. Houze Jr., 2011: Orogenic convection in subtropical South America as seen by the TRMM satellite. *Mon. Wea. Rev.*, **139**, 2399–2420, https://doi.org/10.1175/MWR-D-10-05006.1.

——, and ——, 2016: Convective initiation near the Andes in subtropical South America. *Mon. Wea. Rev.*, **144**, 2351–2374, https://doi.org/10.1175/MWR-D-15-0058.1.

——, M. D. Zuluaga, and R. A. Houze Jr., 2014: Severe convection and lightning in subtropical South America. *Geophys. Res. Lett.*, **41**, 7359–7366, https://doi.org/10.1002/2014GL061767.

——, M. M. Chaplin, M. D. Zuluaga, and R. A. Houze, 2016: Contribution of extreme convective storms to rainfall in South America. *J. Hydrometeor.*, **17**, 353–367, https://doi.org/10.1175/JHM-D-15-0067.1.

Ribeiro, B. Z., and L. F. Bosart, 2018: Elevated mixed layers and associated severe thunderstorm environments in South and North America. *Mon. Wea. Rev.*, **146**, 3–28, https://doi.org/10.1175/MWR-D-17-0121.1.

Roebber, P. J., 2009: Visualizing multiple measures of forecast quality. *Wea. Forecasting*, **24**, 601–608, https://doi.org/10.1175/2008WAF2222159.1.

Romatschke, U., and R. A. Houze, 2010: Extreme summer convection in South America. *J. Climate*, **23**, 3761–3791, https://doi.org/10.1175/2010JCLI3465.1.

Ruiz, J. J., C. Saulo, and J. Nogués-Paegle, 2010: WRF Model sensitivity to choice of parameterization over South America: Validation against surface variables. *Mon. Wea. Rev.*, **138**, 3342–3355, https://doi.org/10.1175/2010MWR3358.1.

Salio, P., M. Nicolini, and A. C. Saulo, 2002: Chaco low-level jet events characterization during the austral summer season. *J. Geophys. Res.*, **107**, 4816, https://doi.org/10.1029/2001JD001315.

——, ——, and E. J. Zipser, 2007: Mesoscale convective systems over southeastern South America and their relationship with the South American low-level jet. *Mon. Wea. Rev.*, **135**, 1290–1309, https://doi.org/10.1175/MWR3305.1.

Satellite Services Division/Office of Satellite Data Processing and Distribution/NESDIS/NOAA/U.S. Department of Commerce, and National Centers for Environmental Prediction/National Weather Service/NOAA/U.S. Department of Commerce, 2004: NCEP ADP Global Upper Air Observational Weather Data, October 1999–continuing. Research Data Archive at the National Center for Atmospheric Research, Computational and Information Systems Laboratory, accessed 10 July 2019, https://doi.org/10.5065/39C5-Z211.

Schumacher, R. S., and R. H. Johnson, 2005: Organization and environmental properties of extreme-rain-producing mesoscale convective systems. *Mon. Wea. Rev.*, **133**, 961–976, https://doi.org/10.1175/MWR2899.1.

——, and ——, 2006: Characteristics of U.S. extreme rain events during 1999–2003. *Wea. Forecasting*, **21**, 69–85, https://doi.org/10.1175/WAF900.1.

——, and C. A. Davis, 2010: Ensemble-based forecast uncertainty analysis of diverse heavy rainfall events. *Wea. Forecasting*, **25**, 1103–1122, https://doi.org/10.1175/2010WAF2222378.1.

——, and A. J. Clark, 2014: Evaluation of ensemble configurations for the analysis and prediction of heavy-rain-producing mesoscale convective systems. *Mon. Wea. Rev.*, **142**, 4108–4138, https://doi.org/10.1175/MWR-D-13-00357.1.

Schwartz, C. S., G. S. Romine, R. A. Sobash, K. R. Fossell, and M. L. Weisman, 2015: NCAR's experimental real-time convection-allowing ensemble prediction system. *Wea. Forecasting*, **30**, 1645–1654, https://doi.org/10.1175/WAF-D-15-0103.1.

Skamarock, W. C., and Coauthors, 2008: A description of the Advanced Research WRF version 3. NCAR Tech. Note NCAR/TN-475+STR, 113 pp., https://doi.org/10.5065/D68S4MVH.

Smith, E. N., J. G. Gebauer, P. M. Klein, E. Fedorovich, and J. A. Gibbs, 2019: The Great Plains low-level jet during PECAN: Observed and simulated characteristics. *Mon. Wea. Rev.*, **147**, 1845–1869, https://doi.org/10.1175/MWR-D-18-0293.1.

Stein, A. F., R. R. Draxler, G. D. Rolph, B. J. B. Stunder, M. D. Cohen, and F. Ngan, 2015: NOAA's HYSPLIT atmospheric transport and dispersion modeling system. *Bull. Amer. Meteor. Soc.*, **96**, 2059–2077, https://doi.org/10.1175/BAMS-D-14-00110.1.

Stensrud, D. J., and J. M. Fritsch, 1993: Mesoscale convective systems in weakly forced large-scale environments. Part I: Observations. *Mon. Wea. Rev.*, **121**, 3326–3344, https://doi.org/10.1175/1520-0493(1993)121<3326:MCSIWF>2.0.CO;2.

Stoelinga, M. T., J. F. Bresch, P. A. Mooney, J. G. Powers, and K. W. Manning, 2018: Users' guide to RIP Version 4.7: A program to visualizing mesoscale model output. National Center for Atmospheric Research Mesoscale & Microscale Meteorology Laboratory, accessed 9 October 2020, http://www2.mmm.ucar.edu/wrf/users/docs/ripug.htm.

Tao, D., and F. Zhang, 2015: Effects of vertical wind shear on the predictability of tropical cyclones: Practical versus intrinsic limit. *J. Adv. Model. Earth Syst.*, **7**, 1534–1553, https://doi.org/10.1002/2015MS000474.

Tewari, M., and Coauthors, 2004: Implementation and verification of the unified Noah land surface model in the WRF model. *20th Conf. on Weather Analysis and Forecasting/16th Conf. on Numerical Weather Prediction*, Seattle, WA, Amer. Meteor. Soc., 14.2a, https://ams.confex.com/ams/84Annual/techprogram/paper_69061.htm.

Thompson, G., P. R. Field, R. M. Rasmussen, and W. D. Hall, 2008: Explicit forecasts of winter precipitation using an improved bulk microphysics scheme. Part II: Implementation of a new

snow parameterization. *Mon. Wea. Rev.*, **136**, 5095–5115, https://doi.org/10.1175/2008MWR2387.1.

Velasco, I., and J. M. Fritsch, 1987: Mesoscale convective complexes in the Americas. *J. Geophys. Res.*, **92**, 9591–9613, https://doi.org/10.1029/JD092iD08p09591.

Vera, C., and Coauthors, 2006: The South American Low-Level Jet Experiment. *Bull. Amer. Meteor. Soc.*, **87**, 63–78, https://doi.org/10.1175/BAMS-87-1-63.

Weisman, M. L., W. C. Skamarock, and J. B. Klemp, 1997: The resolution dependence of explicitly modeled convective systems. *Mon. Wea. Rev.*, **125**, 527–548, https://doi.org/10.1175/1520-0493(1997)125<0527:TRDOEM>2.0.CO;2.

Zhang, C., and Y. Wang, 2017: Projected future changes of tropical cyclone activity over the western North and South Pacific in a 20-km-mesh regional climate model. *J. Climate*, **30**, 5923–5941, https://doi.org/10.1175/JCLI-D-16-0597.1.

——, ——, and K. Hamilton, 2011: Improved representation of boundary layer clouds over the southeast Pacific in ARW-WRF using a modified Tiedtke cumulus parameterization scheme. *Mon. Wea. Rev.*, **139**, 3489–3513, https://doi.org/10.1175/MWR-D-10-05091.1.

Zipser, E. J., D. J. Cecil, C. Liu, S. W. Nesbitt, and D. P. Yorty, 2006: Where are the most intense thunderstorms on Earth? *Bull. Amer. Meteor. Soc.*, **87**, 1057–1072, https://doi.org/10.1175/BAMS-87-8-1057.